



# Mixing and Phytoplankton Growth in an Upwelling System

Antonio Comesaña<sup>1\*</sup>, Bieito Fernández-Castro<sup>2,3</sup>, Paloma Chouciño<sup>1</sup>, Emilio Fernández<sup>1</sup>, Antonio Fuentes-Lema<sup>1</sup>, Miguel Gilcoto<sup>4</sup>, María Pérez-Lorenzo<sup>1</sup> and Beatriz Mouriño-Carballido<sup>1</sup>

<sup>1</sup> Departamento de Biología e Ecoloxía Animal, Universidade de Vigo, Vigo, Spain, <sup>2</sup> Ocean and Earth Sciences, University of Southampton, Southampton, United Kingdom, <sup>3</sup> Physics of Aquatic Systems Laboratory, Margaretha Kamprad Chair, Ecole Polytechnique Fédérale de Lausanne, Institute of Environmental Engineering, Lausanne, Switzerland, <sup>4</sup> Departamento de Oceanografía, Instituto de Investigacións Mariñas (IIM-CSIC), Vigo, Spain

## OPEN ACCESS

### Edited by:

François G. Schmitt,  
UMR8187 Laboratoire D'océanologie  
et de Géosciences (LOG), France

### Reviewed by:

Alejandro Orfila,  
Consejo Superior de Investigaciones  
Científicas (CSIC), Spain  
Qinghua Ye,  
Deltares, Netherlands

### \*Correspondence:

Antonio Comesaña  
ancomesana@uvigo.es

### Specialty section:

This article was submitted to  
Coastal Ocean Processes,  
a section of the journal  
Frontiers in Marine Science

**Received:** 20 May 2021

**Accepted:** 10 August 2021

**Published:** 06 September 2021

### Citation:

Comesaña A, Fernández-Castro B,  
Chouciño P, Fernández E,  
Fuentes-Lema A, Gilcoto M,  
Pérez-Lorenzo M and  
Mouriño-Carballido B (2021) Mixing  
and Phytoplankton Growth in an  
Upwelling System.  
*Front. Mar. Sci.* 8:712342.  
doi: 10.3389/fmars.2021.712342

Previous studies focused on understanding the role of physical drivers on phytoplankton bloom formation mainly used indirect estimates of turbulent mixing. Here we use weekly observations of microstructure turbulence, dissolved inorganic nutrients, chlorophyll *a* concentration and primary production carried out in the Ría de Vigo (NW Iberian upwelling system) between March 2017 and May 2018 to investigate the relationship between turbulent mixing and phytoplankton growth at different temporal scales. In order to interpret our results, we used the theoretical framework described by the Critical Turbulent Hypothesis (CTH). According to this conceptual model if turbulence is low enough, the depth of the layer where mixing is active can be shallower than the mixed-layer depth, and phytoplankton may receive enough light to bloom. Our results showed that the coupling between turbulent mixing and phytoplankton growth in this system occurs at seasonal, but also at shorter time scales. In agreement with the CTH, higher phytoplankton growth rates were observed when mixing was low during spring-summer transitional and upwelling periods, whereas low values were described during periods of high mixing (fall-winter transitional and downwelling). However, low mixing conditions were not enough to ensure phytoplankton growth, as low phytoplankton growth was also found under these circumstances. Wavelet spectral analysis revealed that turbulent mixing and phytoplankton growth were also related at shorter time scales. The higher coherence between both variables was found in spring-summer at the ~16–30 d period and in fall-winter at the ~16–90 d period. These results suggest that mixing could act as a control factor on phytoplankton growth over the seasonal cycle, and could be also involved in the formation of occasional short-lived phytoplankton blooms.

**Keywords:** phytoplankton, turbulent mixing, critical turbulence hypothesis, wavelet analysis, Ría de Vigo, NW Iberian upwelling system

## 1. INTRODUCTION

Marine phytoplankton is responsible for about half of the primary production in the biosphere (Field et al., 1998), and therefore plays a key role in the cycling of matter and energy on Earth. The two main resources limiting phytoplankton growth, light, and nutrients availability, are strongly dependent on turbulent mixing conditions in the water column. By controlling the vertical

displacement of cells, mixing determines their exposure to solar photosynthetic active radiation. In addition, turbulent mixing is one of the mechanisms responsible for the supply of inorganic nutrients from deep waters to the surface, where they can be taken up by phytoplankton. For this reason, turbulent mixing has been frequently invoked in the formulation of theoretical models, either to explain the dominance of different phytoplankton functional groups (Margalef, 1978) or the behavior of individual phytoplankton cells (Sverdrup, 1953).

The Critical Depth Hypothesis (CDH) formulated by Sverdrup (1953) to explain the onset of the North Atlantic spring bloom, pioneered the development of conceptual models relating phytoplankton growth, mixing conditions, and light availability. The CDH concluded that deep mixed-layers during winter keep phytoplankton in an unfavorable light environment and therefore limit their production. When solar heating thins the non-stratified mixed-layer, phytoplankton could have the potential to bloom because growth outweighs losses due to the increase of solar exposure. He defined the “critical depth” as the lower limit of the water column in which depth-integrated production of organic matter equals its oxidation by respiratory processes. Since its formulation, several studies have attempted to verify the CDH in the field with controversial results. Some of them found evidence supporting the CDH (Semina, 1960; Menzel and Ryther, 1961; Nelson and Smith, 1991; Obata et al., 1996; Siegel et al., 2002; Chiswell, 2011; Brody et al., 2013; Chiswell et al., 2013, 2015; Brody and Lozier, 2014, 2015; Wihsgott et al., 2019; Hopkins et al., 2021), whereas others rejected it based on the observation that phytoplankton growth rate was positive during deep winter mixing (Acuña et al., 2010; Behrenfeld, 2010; Boss and Behrenfeld, 2010; Behrenfeld et al., 2013; Behrenfeld and Boss, 2014; Arteaga et al., 2020). A recent study revealed that although phytoplankton starts growing in early winter at weak rates, a proper bloom initiates only in spring when atmospheric cooling subsides and the mixed-layer rapidly shoals (Mignot et al., 2018). The observation that phytoplankton blooms sometimes occur in the apparent absence of water column stratification (Townsend et al., 1992; Ellertsen, 1993; Backhaus et al., 1999; Körtzinger et al., 2008) led to propose alternative bloom formation processes (Franks, 2015). The Critical Turbulence Hypothesis (CTH, Huisman et al., 1999a,b) proposed that if turbulence is low enough, phytoplankton in the well-lit surface layer could bloom independently of the thickness of the mixed-layer.

Sverdrup (1953) was aware of the distinction between a mixed-layer, defined as a subsurface layer of relatively uniform temperature or density, and the active mixed-layer, defined by the intensity of turbulent diffusivity ( $K$ ). However, by explicitly assuming that it was large enough to be ignored, he avoided the need to include  $K$  in his model. Franks (2015) emphasized that using the theoretical background of the CDH requires observations of microstructure turbulence, rather than mixed-layer depth estimates derived from thermohaline properties. He also noted that it is crucial to determine, not only the intensity of turbulence, but also its vertical structure and temporal variability. In a recent study Hopkins et al. (2021) employed 2 weeks of sub-hourly observations of turbulent kinetic

energy dissipation rate to demonstrate the critical role that the strength and structure of turbulent mixing play in governing the development of spring phytoplankton blooms in the Celtic Sea. According to these authors their results could be applicable to any region where wind-driven mixing can modify nutrient and light availability.

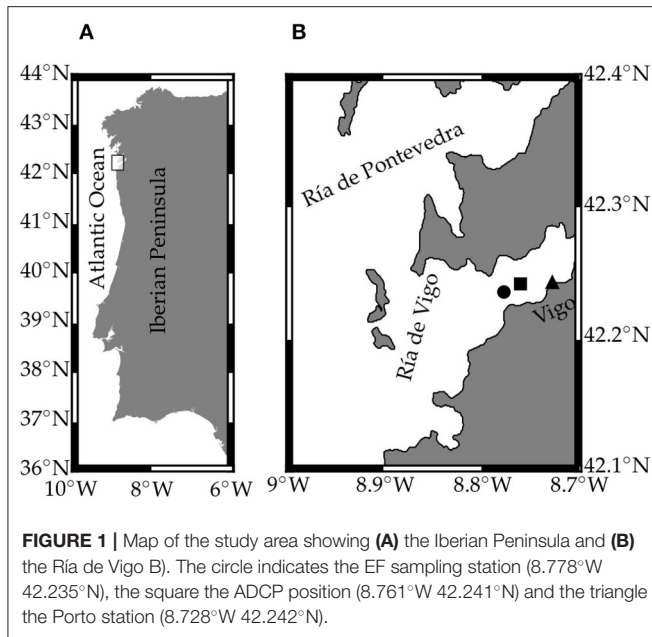
Eastern boundary upwelling systems (EBUS) are complex regions where the interaction between hydrographic conditions and phytoplankton growth occurs within a broad range of temporal scales (Pitcher et al., 2010). Several studies have investigated the role of the major physical processes that may control biological productivity in these regions (Messié and Chavez, 2015). Patti et al. (2008) suggested that several driving factors, as nutrients concentration, light availability, shelf extension, and surface turbulence estimated from wind speed, must be considered when investigating the phytoplankton biomass distribution. By using Finite Size Lyapunov Exponents and satellite data, Rossi et al. (2009) described a global negative correlation between surface horizontal mixing and chlorophyll. Fearon et al. (2020) used a 1D modeling approach to predict vertical mixing from wind speed in St Helena Bay (Bengala upwelling system), and emphasized the role of land-sea breeze in the development of phytoplankton blooms. As far as we know direct observations of microstructure turbulence have been never used to investigate the role of mixing in phytoplankton bloom formation in EBUS.

The Ría de Vigo is a long narrow embayment located in the northern boundary of the Canary Current upwelling ecosystem. Intense and intermittent upwelling events occur mainly in spring and summer (Fraga, 1981). In these seasons, the prevailing northerly winds cause offshore Ekman transport of surface water, and the rise of cold nutrient-enriched subsurface waters, which stimulate phytoplankton growth and support a highly productive pelagic ecosystem (Fréon et al., 2009). During winter, southerly winds driving downwelling conditions are dominant. The annual cycle of phytoplankton biomass corresponds to a typical temperate shelf sea, with the development of spring and autumn blooms (Álvarez-Salgado et al., 1996; Nogueira et al., 1997; Moncoiffe et al., 2000; Cermeño et al., 2006). On the other hand, short-term variability of the upwelling regime and runoff water pulses induce changes on phytoplankton biomass and composition over shorter time-scales (Nogueira et al., 2000; Nogueira and Figueiras, 2005). The main goal of this study is to investigate the relationship between vertical turbulent mixing and phytoplankton growth at the different temporal scales involved in the coupling between physical and biological processes in this coastal upwelling system.

## 2. MATERIALS AND METHODS

### 2.1. Sampling Site

In the framework of the REMEDIOS project (RoLE of Mixing on phytoplankton bloom initiation, maintenance, and DIssipatiOn in the Galician ríaS, <http://proyectorremedios.com/inicio>), 52 samplings were carried out on board R/V Kraken at station EF located in the inner part of the Ría de Vigo (8.778°W 42.235°N, ~45 m depth, **Figure 1**), from 9 March 2017 to 10 May



2018, approximately once a week. During each sampling, hydrographic, and microstructure turbulence profiles, as well as samples for the determination of inorganic nutrients, chlorophyll *a*, and primary production were collected. A continuous recording of current velocity profiles during the sampling period was acquired with an upward-looking bottom-moored Acoustic Doppler Current Profiler (ADCP). The weekly samplings were clustered into three groups by virtue of the predominance of upwelling (U), downwelling (D), or the transition between both conditions (T). This classification was based on the upwelling index (UI), the horizontal currents, and hydrographic information. The upwelling index was calculated as the offshore Ekman transport (Bakun, 1973) in the direction perpendicular to the shoreline (Gomez-Gesteira et al., 2006):

$$UI = -\frac{\rho_a c_d W W_y}{\rho f} \quad (1)$$

being *f* the Coriolis factor, *c<sub>d</sub>* the drag coefficient, *ρ<sub>a</sub>* and *ρ* the air and seawater density, respectively, and *W* and *W<sub>y</sub>* the wind speed and the magnitude of the north-south component. UI data for the Rías Baixas region (SW of Galicia) were obtained from the website of the Instituto Español de Oceanografía ([www.indicedeafloresamiento.ieo.es](http://www.indicedeafloresamiento.ieo.es)). UI is calculated from sea-level pressure of the WRF (Weather Research and Forecasting, <http://www2.mmm.ucar.edu/wrf/users/>) atmospheric model from Meteogalicia ([www.meteogalicia.gal](http://www.meteogalicia.gal)). Daily solar irradiance (*I<sub>0</sub>*) data were obtained from the Porto station of Meteogalicia (Figure 1), located at the inner part of the Ría de Vigo (8.728°W 42.242°N). Photosynthetically active radiation (PAR) at the surface was computed as a fraction of *I<sub>0</sub>* following PAR = 0.43 × *I<sub>0</sub>* (Morel, 1988).

## 2.2. Hydrography and Turbulence

Hydrographic and turbulent data were collected with a microstructure turbulence profiler MSS90 (Prandke and Stips, 1998). The profiler was equipped with two microstructure shear sensors (type PNS06), a microstructure temperature sensor (FP07), a high-precision CTD (Conductivity-Temperature-Depth) probe, a fluorescence sensor, and an accelerometer. On each sampling day, 10 profiles were conducted and then averaged. The profiler was balanced to have negative buoyancy in the water column and a sinking velocity in the range 0.4–0.7 m s<sup>-1</sup>.

Dissipation rates of turbulent kinetic energy (*ε*) were computed in 512 data point segments, with 50% overlap, from the vertical shear (*∂<sub>z</sub>u*) variance using the Taylor (1935) equation assuming isotropic turbulence:

$$\epsilon = \frac{15}{2} \nu \langle (\partial_z u)^2 \rangle \quad (2)$$

where *ν* is the kinematic viscosity of seawater and *⟨⟩* denotes the ensemble average. The shear variance was computed by integrating the shear power spectrum. The lower integration limit was set to 2 cpm. The upper cut-off wavenumber for the integration of the shear spectrum was set as the Kolmogoroff number *k<sub>c</sub>* = (2π)<sup>-1</sup> *ε*<sup>1/4</sup> *ν*<sup>-3/4</sup>. An iterative procedure was applied to determine *k<sub>c</sub>*. The maximum upper cut-off was not allowed to exceed 30 cpm to avoid the noisy part of the spectrum. Assuming a universal form of the shear spectrum, *ε* was corrected for the loss of variance below and above the integration limits, using the polynomial functions reported by Prandke et al. (2000). *ε* values were then averaged in 1 m bins. Peaks due to particle collisions were removed by comparing the dissipation computed simultaneously from the two shear sensors. The turbulent diffusivity *K* was estimated from the Osborn (1980) formula:

$$K = \gamma \frac{\epsilon}{N^2} \quad (3)$$

where *N*<sup>2</sup> is the squared buoyancy frequency and *γ* is the mixing efficiency, here considered to be 0.2 (Oakey, 1982). Although a growing body of evidence suggests that *γ* is not always constant, we follow the recommendation of Gregg et al. (2018) to use *γ* = 0.2 for microstructure studies until observations, laboratory experiments, and numerical simulations converge on a more accurate formulation. Furthermore, the Ría de Vigo is a system characterized by being marginally unstable to shear-driven turbulence (Fernández-Castro et al., 2018), which justifies the choice of this *γ* value (Smyth, 2020).

The mixed-layer depth (MLD) was determined as the depth where an increase of 0.125 kg m<sup>-3</sup> was observed with respect to the surface values (~2 m). The turbulent layer depth (TLD) was computed using one-dimensional lagrangian simulations forced with the observed diffusivity profiles (Ross and Sharples, 2004). The new particle depth (*z<sub>n+1</sub>*) was computed in based of the present depth (*z<sub>n</sub>*) after:

$$z_{n+1} = z_n + \Delta t \partial_z K(z_n) + R \sqrt{\frac{2 \Delta t K (z_n + \frac{1}{2} \Delta t \partial_z K(z_n))}{r}} \quad (4)$$

where  $R \in [-1, 1]$  is a random number of variance  $r = \frac{1}{3}$  and  $\Delta t$  the time-step chosen by ensuring that it was much lower than the minimum value of  $|(\partial_{zz}K)^{-1}|$ . In these simulations, 1,000 particles were released at the surface and let evolve in the diffusivity field for 24 h. The TLD was defined as the lower limit of the depth range containing 95% of 1,000 particles at the end of the simulation. The light availability was computed as the daily-average surface PAR in the turbulent layer computed following the expression reported in (Vallina and Simó, 2007):

$$LA = PAR \times \frac{1 - e^{-\kappa TLD}}{\kappa TLD} \quad (5)$$

where  $\kappa$  is the light attenuation coefficient determined from PAR profiles obtained with a Licor PAR sensor on each sampling day.

### 2.3. Current Velocities

The RD Instruments Acoustic Doppler Current Profiler (ADCP) was bottom-moored in the central part of the Ría de Vigo close to the EF station (8.761° W 42.241° N, ~ 45 m depth, **Figure 1**). Profiles of current velocity were acquired continuously from 3 March 2017 to 29 May 2018. A gap in data collection occurred from 30 May 2017 to 8 June 2017 due to maintenance operations. The measurements were made in 89 layers with a bin thickness of 0.5 m and the first bin located at 2 m above the ADCP transducers. Every 10 min, 85 samples of 3D currents were acquired at 2 Hz, averaged in ensemble and recorded. Resulting zonal and meridional velocity vector components were projected into the axis along the main channel (35° north of east) of the Ría de Vigo. Hence, the along-Ría component was positive into the Ría. Finally, these time-series were smoothed with the  $\mathcal{A}_{24}^2 \mathcal{A}_{25}$  operator (Godin, 1972), which applies three consecutive moving averages with window size of 24, 24, and 25 h, with the aim of filtering out the tidal and supertidal frequencies. The residual current velocity along the main axis of the Ría at 32 m depth ( $u_{32}$ ) was selected to characterize the deep circulation in the Ría. Positive (negative) values indicate the deep water inflow (outflow) into the Ría and surface water outflow (inflow), corresponding to upwelling and downwelling conditions, respectively.

### 2.4. Inorganic Nutrients Concentration

Samples for the determination of dissolved inorganic nutrients (nitrate, nitrite, ammonium, phosphate, and silica) were collected from 8 to 9 depths, in the water column by using 5 l Niskin bottles. Samples were frozen at  $-20^\circ\text{C}$  until further determination at the laboratory, following the methods described by Hansen and Koroleff (2007).

### 2.5. Nutrient Supply

Nutrient input into the surface layer of the Rías occurs mainly by coastal upwelling, while continental runoff and precipitation (Fernández et al., 2016) and turbulent diffusion (Moreira-Coello et al., 2017) represent minor inputs. An estimate of the supply of nitrate due to upwelling pulses was computed as the nitrate

vertical advection induced by convergence of upwelled waters inside the Ría:

$$\Phi_a(\text{NO}_3^-) = \begin{cases} \text{UI} \frac{l}{A} \text{NO}_3^-(40) & \text{UI} > 0 \\ 0 & \text{UI} < 0 \end{cases} \quad (6)$$

where  $l$  and  $A$  are the length of the mouth and surface area of the Ría (~ 10 km and ~ 174 km<sup>2</sup>, respectively), and  $\text{NO}_3^-(40)$  is the nitrate concentration at the deepest sampling depth around 40 m depth. UI is the upwelling index averaged over the 3 days prior each sampling (Gilcoto et al., 2017). A null value was assigned to those samplings under downwelling conditions.

### 2.6. Chlorophyll *a* Concentration and Primary Production Rates

Chlorophyll *a* concentration (Chl *a*) and primary production rates were determined from samples collected at surface (~0.5–1 m) and 10 m depth. For the determination of total Chl *a*, 250 ml of seawater were filtered through polycarbonate filters of 0.2  $\mu\text{m}$ , which were later frozen at  $-20^\circ\text{C}$  until analysis. The fluorescence (Fluo) emitted by the Chl *a* was measured from pigments extracted in 90% acetone at  $4^\circ\text{C}$  overnight using a Turner designs Trilogy fluorometer previously calibrated with pure Chl *a*. The measured Chl *a* concentrations were used to calibrate the MSS fluorometer by using a linear regression ( $\text{Chl } a = 1.47 \times \text{Fluo} - 0.16$ ,  $R^2 = 0.89$ ,  $n = 22$ ) for Chl *a* concentration ranging between 0.26 and 5.83 mg m<sup>-3</sup>.

Primary production rates were determined by running incubations with the radioisotope <sup>14</sup>C as described in Cermeño et al. (2016). Briefly, four 72 ml acid-washed polystyrene bottles (three light and one dark bottle) were filled with seawater from each depth. Each bottle was inoculated with ~ 5  $\mu\text{Ci}$  of  $\text{NaH}^{14}\text{CO}_3$  and then incubated for 2 h starting at noon. An incubator equipped with a set of blue and neutral density plastic filters was used to simulate irradiance conditions at the original sampling depths. Temperature conditions during the incubation period were kept similar to those observed at surface ( $\pm 1.5^\circ\text{C}$ ) by employing a closed refrigerated water system. Immediately after incubation, samples were filtered through 0.2  $\mu\text{m}$  polycarbonate filters under low-vacuum pressure. Non-assimilated radioactive inorganic carbon retained in the filters was removed by exposing them to concentrated HCl fumes overnight. Radioactivity signal on each sample was determined on a 1409-012 Wallac scintillation counter, which used an internal standard for quenching correction.

Growth rates ( $\mu$ ) were computed as the ratio primary production to phytoplankton biomass. Carbon phytoplankton biomass was estimated assuming the C:Chl *a* ratios for three hydrographic conditions in the Ría de Vigo: stratification ( $55 \pm 13$ ), winter mixing ( $54 \pm 27$ ) and upwelling ( $35 \pm 18$ ) at the same station (Cermeño et al., 2005). In our case  $35 \pm 18$  was used for upwelling and  $55 \pm 30$  for downwelling and transitional periods. Daily growth rates were computed from hourly values considering the number of light hours on the sampling day.

## 2.7. Wavelet Analysis

Time-series of phytoplankton growth rates and turbulent layer depth were analyzed with the wavelet transform, a technique in which the evolution of the time-series variance is analyzed at different frequencies. The contribution of variance at different times and periods was determined by the wavelet power spectrum (WPS), which was represented in the time-period plane, the periodogram (Cazelles et al., 2008). The finite length of time-series provokes discontinuities at their borders delimited by the cone of influence, in which the edge effects are negligible (Torrence and Compo, 1998). The relation of two time-series can be identified in time and period in terms of coherence ( $\Gamma^2$ , Liu, 1994), from 0 to 1 due to a smoothing in both time and period following the recommendation of Torrence and Webster (1999). Peaks in the spectrum can be assumed to be a true feature with a certain confidence by using a test against an assumed background level (Torrence and Compo, 1998). In this case, the background was simulated with 1000 replicas of surrogate time-series by using a hidden Markov model (HMM), in which the short-term temporal correlation of the original time-series is preserved (Cazelles and Stone, 2003). The null hypothesis tested is that the original and surrogate time-series had same value distribution and short-term autocorrelation (Cazelles et al., 2014) with 95% confidence level.

To apply the wavelet transform, the time-series have to be spaced in a regular time interval ( $\delta t$ ). Hence, phytoplankton growth rates and turbulent layer depth were linearly interpolated onto an equi-spatially time-grid with  $\delta t \approx 8$  d and  $N = 52$  points. The comparison between time-series was ensured by using the standardization of the variables, so they had nil mean and unit variance. An specific code was built on Python in order to conduct the wavelet analysis.

## 3. RESULTS

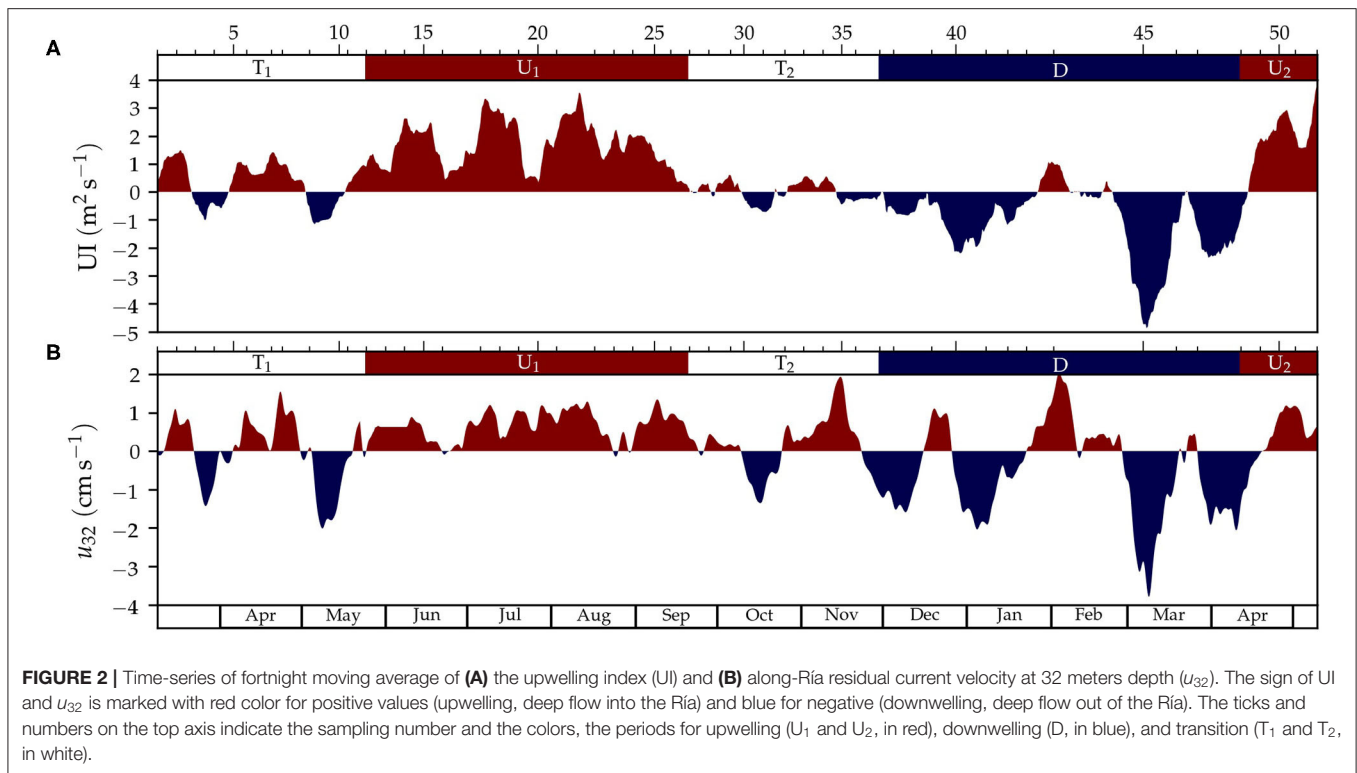
### 3.1. Environmental and Hydrographic Conditions

The temporal variability of the smoothed (fortnight moving average) upwelling index and the smoothed current velocity sampled at 32 m depth allowed us to establish upwelling, downwelling, or transitional periods (Figure 2). Based on the bidirectional circulation of the Ría de Vigo, positive values of UI and deep current velocity correspond with the input of deep water, and negative values with the output of deep water. From sampling 1 to 11 (9 Mar 2017–18 May 2018) a spring transitional period ( $T_1$ ) was sampled characterized by the alternation of relatively short upwelling and downwelling events, which resulted in low averaged upwelling index of  $UI = 0.3 \pm 0.1 \text{ m}^2 \text{ s}^{-1}$  (mean  $\pm$  standard uncertainty of the mean, Table 1). Samplings 12–26 (25 May 2017 to 14 Sep 2017), when the averaged upwelling index was positive ( $UI = 1.7 \pm 0.1 \text{ m}^2 \text{ s}^{-1}$ ), were characterized by spring-summer upwelling conditions ( $U_1$ ). Samplings 27–36 (21 Sep 2017–21 Nov 2017) recorded a fall transitional period ( $T_2$ ), with alternation of upwelling and downwelling events and null averaged upwelling index ( $UI = 0.0 \pm 0.1 \text{ m}^2 \text{ s}^{-1}$ ). Between

late fall and early spring (samplings 34–47, 30 Nov 2017–27 Mar 2018), downwelling conditions were dominant (D) and averaged upwelling index was negative ( $UI = -1.1 \pm 0.1 \text{ m}^2 \text{ s}^{-1}$ ). Finally, in spring 2018 (samplings 48–52, 12 Apr 2018–10 May 2018) the beginning of the spring upwelling season ( $U_2$ ) was sampled, characterized by a mean upwelling index ( $UI = 1.9 \pm 0.4 \text{ m}^2 \text{ s}^{-1}$ ) similar to the previous upwelling period ( $U_1$ ).

The variability in hydrographic properties sampled by the microstructure turbulence profiler is shown in Figures 3A–F and Table 1. The spring transitional period  $T_1$  (March–May 2017) was characterized by relatively low ( $14\text{--}15^\circ\text{C}$ ) and vertically homogeneous temperature. In general, salinity was relatively low at the surface ( $34.6 \pm 0.2$ ), which caused intermediate values of the mean squared buoyancy frequency ( $N^2$ ,  $1.4 \pm 0.3 \times 10^{-4} \text{ s}^{-2}$ ). Averaged dissipation rates ( $\epsilon$ ) in the water column were relatively large ( $9 \pm 5 \times 10^{-8} \text{ W kg}^{-1}$ ), which combined with intermediate  $N^2$  values caused intermediate values of averaged diffusivity ( $K$ ,  $6 \pm 3 \times 10^{-4} \text{ m}^2 \text{ s}^{-1}$ ). During the spring-summer upwelling period  $U_1$  (May–September 2017), surface temperature was relatively high whereas salinity was rather homogeneous in the water column. The thermal vertical gradient resulted in intermediate  $N^2$  values ( $1.8 \pm 0.2 \times 10^{-4} \text{ s}^{-2}$ ), whereas  $\epsilon$  ( $3.5 \pm 0.7 \times 10^{-8} \text{ W kg}^{-1}$ ) and  $K$  ( $1.6 \pm 0.3 \times 10^{-4} \text{ m}^2 \text{ s}^{-1}$ ) were comparatively low. The fall transitional period  $T_2$  (September–November 2017) was characterized by a decrease in surface temperature ( $15.1 \pm 0.3^\circ\text{C}$ ), and relatively homogeneous vertical salinity distribution ( $35.57\text{--}35.70$ ). The weak thermal stratification caused low  $N^2$  values ( $1.1 \pm 0.2 \times 10^{-4} \text{ s}^{-2}$ ). Dissipation rates were relatively low ( $5 \pm 1 \times 10^{-8} \text{ W kg}^{-1}$ ), but the low  $N^2$  values provoked the highest values of  $K$  ( $40 \pm 20 \times 10^{-4} \text{ m}^2 \text{ s}^{-1}$ ). This increase was mainly due to the high values computed at depths greater than  $\sim 20$  m in sampling 31 (18 Oct 2017,  $K = 146 \times 10^{-4} \text{ m}^2 \text{ s}^{-1}$ ), and above  $\sim 30$  m in sampling 36 (21 Nov 2017,  $K = 191 \times 10^{-4} \text{ m}^2 \text{ s}^{-1}$ ). During the winter downwelling period D (December 2017–March 2018), low surface temperature ( $12.9 \pm 0.1^\circ\text{C}$ ) and surface salinity ( $33.9 \pm 0.5$ ) were registered. This period was characterized by intense haline vertical stratification, which caused high  $N^2$  values ( $2.3 \pm 0.8 \times 10^{-4} \text{ s}^{-2}$ ). Dissipation rates were relatively high ( $8 \pm 3 \times 10^{-8} \text{ W kg}^{-1}$ ), giving rise to high  $K$  ( $20 \pm 10 \times 10^{-4} \text{ m}^2 \text{ s}^{-1}$ ). During this period, high  $K$  values were calculated throughout the water column in sampling 38 (5 Dec 2017,  $K = 150 \times 10^{-4} \text{ m}^2 \text{ s}^{-1}$ ). The spring 2018 upwelling period  $U_2$  (March–May 2018) presented low surface temperature ( $13.8 \pm 0.3^\circ\text{C}$ ) and surface salinity ( $33 \pm 1$ ). The thermal, and specially, the haline vertical gradients, caused high  $N^2$  values ( $3 \pm 2 \times 10^{-4} \text{ s}^{-2}$ ). Dissipation rates were relatively high ( $9 \pm 2 \times 10^{-8} \text{ W kg}^{-1}$ ), which, combined with the high  $N^2$  values, yielded intermediate  $K$  values ( $6 \pm 2 \times 10^{-4} \text{ m}^2 \text{ s}^{-1}$ ).

The turbulent layer depth (TLD), an indication of the depth reached by currently active mixing (Brainerd and Gregg, 1995) computed by simulations forced with  $K$  profiles (see section 2), was significantly correlated with the mixed-layer depth ( $TLD = 0.48 \times MLD + 5.4$ ,  $R^2 = 0.66$ ,  $p < 0.001$ ,  $n = 52$ ), and exhibited similar seasonal variability (Figure 3). As a result of the enhanced  $K$  during samplings 36 and 38, maximum TLD values were computed during the fall transitional  $T_2$  ( $13 \pm 2$  m) and winter



downwelling D ( $12 \pm 3$  m) periods, whereas TLD was shallower during the spring-summer upwelling  $U_1$  ( $7.1 \pm 0.4$  m). Most observations ( $n = 40$ ) corresponded to shallow ( $< 9$  m) MLD coinciding with slightly deeper (3–4 m) TLD. This could be the result of the limited number of microstructure turbulence data near the surface used for the calculation of both TLD and MLD. For samplings showing relatively deep mixed-layers (MLD  $> 9$  m,  $n = 12$ ), TLD was  $8 \pm 2$  m shallower than MLD in average. In fact, in four sampling days, TLD was at least 12 m shallower than MLD (samplings 3, 31, 36, and 37), which suggests the occurrence of mixed-layers that were not actively mixing at the time of sampling.

### 3.2. Inorganic Nutrients

The temporal variability of the vertical distribution of nitrate is shown in **Figure 3G** and **Table 1**. During the spring transitional period  $T_1$ , nitrate concentrations in surface ( $2.2 \pm 0.8 \mu\text{M}$ ) and deep waters ( $4.1 \pm 0.7 \mu\text{M}$ ) were relatively low. Nitrate concentration increased on average during the spring-summer upwelling  $U_1$  at deep waters ( $7.8 \pm 0.7 \mu\text{M}$ ), whereas lower concentrations were found at the surface ( $0.3 \pm 0.2 \mu\text{M}$ ). The fall transitional period  $T_2$  was characterized by increasing nitrate concentrations both at surface ( $5 \pm 1 \mu\text{M}$ ) and deep waters ( $10.0 \pm 0.9 \mu\text{M}$ ). Nitrate concentration increased during the winter downwelling D at the surface ( $10.9 \pm 0.7 \mu\text{M}$ ) but it decreased in deep layers ( $7.2 \pm 0.6 \mu\text{M}$ ). Finally, the spring upwelling  $U_2$  was characterized by declining nitrate concentrations at surface ( $2 \pm 1 \mu\text{M}$ ) and deep layers ( $6.0 \pm 0.7 \mu\text{M}$ ). Distinctive patterns in nitrate distribution were observed in samplings characterized by enhanced  $K$  (samplings 36 and 38). During

these samplings, enhanced nitrate concentrations ( $\geq 9 \mu\text{M}$ ) were sampled throughout the water column, coinciding with fall upwelling conditions.

Additional information about the vertical distribution of nitrite, ammonium, phosphate and silicate is shown in **Supplementary Figure 1**. In general, the seasonal variability of nitrite, phosphate and silicate concentration were very similar to the described nitrate distribution. In fact, a statistically significant positive relationship was found between nitrate and nitrite ( $\text{NO}_2^- = 0.062 \times \text{NO}_3^- + 0.11$ ,  $R^2 = 0.56$ ,  $p < 0.001$ ,  $n = 428$ ), phosphate ( $\text{PO}_4^{3-} = 0.060 \times \text{NO}_3^- + 0.21$ ,  $R^2 = 0.74$ ,  $p < 0.001$ ,  $n = 428$ ) and silicate ( $\text{Si} = 0.68 \times \text{NO}_3^- + 0.4$ ,  $R^2 = 0.73$ ,  $p < 0.001$ ,  $n = 428$ ). However, no statistically significant relationship was found between nitrate and ammonium concentration ( $R^2 = 0.11$ ,  $p < 0.001$ ,  $n = 428$ ). Surface waters exhibited higher averaged ammonium concentration during winter downwelling during winter downwelling ( $3.6 \pm 0.7 \mu\text{M}$ ), whereas during the other periods values ranged between  $0.66 \pm 0.08 \mu\text{M}$  ( $U_2$ ) and  $2.4 \pm 0.4 \mu\text{M}$  ( $T_2$ ). The seasonal variability of ammonium concentrations at deep waters was low ( $2.0$ – $2.8 \mu\text{M}$ ).

### 3.3. Chlorophyll *a*, Primary Production and Phytoplankton Growth Rates

The temporal and vertical distribution of Chl *a* concentration, determined from the calibrated fluorescence sensor included in the microstructure turbulence profiler, is shown in **Figure 3H**. Relatively large short-term variability was observed for the depth of the Chl *a* maximum, which was shallower and less variable during the upwelling periods ( $14 \pm 2$  m during  $U_1$  and  $8 \pm 3$  m

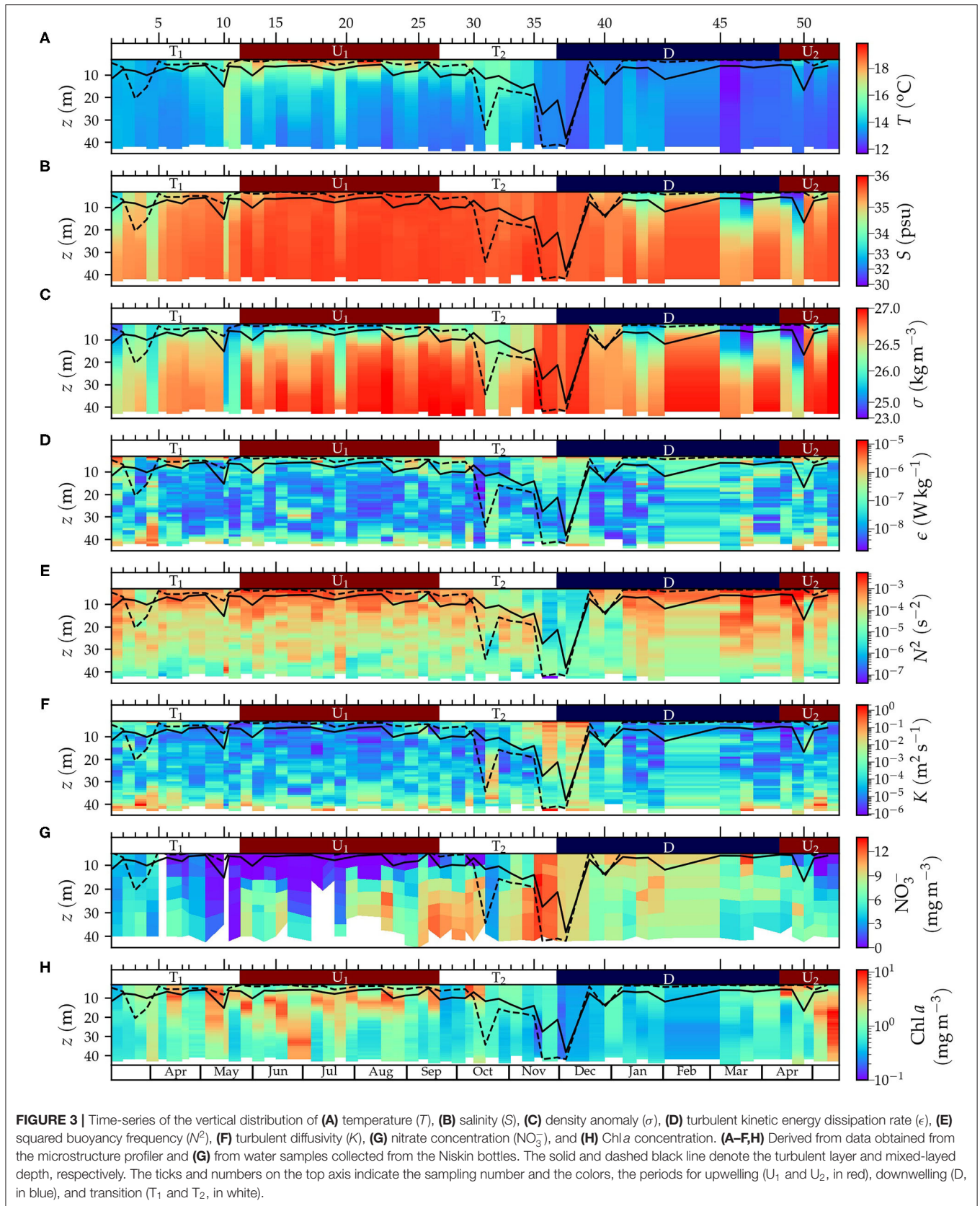


**TABLE 1** | Mean  $\pm$  standard uncertainty of the mean for selected variables averaged on each time periods.

Variable	Units	T <sub>1</sub> (n = 11)	U <sub>1</sub> (n = 15)	T <sub>2</sub> (n = 10)	D (n = 11)	U <sub>2</sub> (n = 5)	Tukey comparisons
UI	m <sup>2</sup> s <sup>-1</sup>	0.3 $\pm$ 0.1	1.7 $\pm$ 0.1	-0.0 $\pm$ 0.1	-1.1 $\pm$ 0.1	1.9 $\pm$ 0.4	D < T <sub>1</sub> , T <sub>2</sub> < U <sub>1</sub> , U <sub>2</sub>
T <sub>0</sub>	°C	14.8 $\pm$ 0.4	17.8 $\pm$ 0.3	15.1 $\pm$ 0.3	12.9 $\pm$ 0.1	13.8 $\pm$ 0.3	D < T <sub>1</sub> , T <sub>2</sub> , U <sub>1</sub> ; U <sub>2</sub> < U <sub>1</sub>
T <sub>32</sub>	°C	14.0 $\pm$ 0.4	13.5 $\pm$ 0.1	13.6 $\pm$ 0.2	13.1 $\pm$ 0.2	12.80 $\pm$ 0.05	
S <sub>0</sub>	psu	34.6 $\pm$ 0.2	35.50 $\pm$ 0.06	35.57 $\pm$ 0.03	33.9 $\pm$ 0.5	33 $\pm$ 1	D, U <sub>2</sub> < T <sub>2</sub> , U <sub>2</sub> ; U <sub>2</sub> < T <sub>1</sub>
S <sub>32</sub>	psu	35.33 $\pm$ 0.09	35.73 $\pm$ 0.01	35.70 $\pm$ 0.02	35.50 $\pm$ 0.05	35.3 $\pm$ 0.2	D < U <sub>1</sub> ; T <sub>1</sub> , U <sub>2</sub> < T <sub>2</sub> U <sub>1</sub>
N <sup>2</sup>	10 <sup>-4</sup> $\times$ s <sup>-2</sup>	1.4 $\pm$ 0.3	1.8 $\pm$ 0.2	1.1 $\pm$ 0.2	2.3 $\pm$ 0.8	3 $\pm$ 2	
N <sub>max</sub> <sup>2</sup>	10 <sup>-4</sup> $\times$ s <sup>-2</sup>	10 $\pm$ 2	20 $\pm$ 4	4.0 $\pm$ 0.9	20 $\pm$ 5	38 $\pm$ 9	T <sub>2</sub> < D, U <sub>1</sub> , U <sub>2</sub> ; T <sub>1</sub> < U <sub>2</sub>
MLD	m	8 $\pm$ 2	4.2 $\pm$ 0.2	17 $\pm$ 4	12 $\pm$ 5	4.1 $\pm$ 0.6	U <sub>1</sub> < T <sub>2</sub>
TLD	m	8.6 $\pm$ 0.9	7.1 $\pm$ 0.4	13 $\pm$ 2	12 $\pm$ 3	9 $\pm$ 3	
PAR	W m <sup>-2</sup>	100 $\pm$ 3	115 $\pm$ 3	55 $\pm$ 3	41 $\pm$ 2	107 $\pm$ 7	D < T <sub>2</sub> < T <sub>1</sub> , U <sub>1</sub> , U <sub>2</sub> ; U <sub>1</sub> < T <sub>1</sub>
LA	W m <sup>-2</sup>	46 $\pm$ 6	61 $\pm$ 5	25 $\pm$ 5	19 $\pm$ 4	52 $\pm$ 8	D, T <sub>2</sub> < T <sub>1</sub> , U <sub>2</sub> ; D < U <sub>1</sub>
ε	10 <sup>-8</sup> $\times$ W kg <sup>-1</sup>	9 $\pm$ 5	3.5 $\pm$ 0.7	5 $\pm$ 1	8 $\pm$ 3	9 $\pm$ 2	
K	10 <sup>-4</sup> $\times$ m <sup>2</sup> s <sup>-1</sup>	6 $\pm$ 3	1.6 $\pm$ 0.3	40 $\pm$ 20	20 $\pm$ 10	6 $\pm$ 2	
NO <sub>3</sub> <sup>-</sup> (0)	mmol m <sup>-3</sup>	2.2 $\pm$ 0.8	0.3 $\pm$ 0.2	5 $\pm$ 1	10.9 $\pm$ 0.7	2 $\pm$ 1	T <sub>1</sub> , T <sub>2</sub> , U <sub>1</sub> , U <sub>2</sub> < D; U <sub>1</sub> < T <sub>2</sub>
NO <sub>3</sub> <sup>-</sup> (32)	mmol m <sup>-3</sup>	4.1 $\pm$ 0.7	7.8 $\pm$ 0.7	10.0 $\pm$ 0.9	7.2 $\pm$ 0.6	6.0 $\pm$ 0.7	U <sub>2</sub> < T <sub>2</sub> < D; T <sub>1</sub> < D, T <sub>2</sub> , U <sub>1</sub>
NO <sub>2</sub> <sup>-</sup> (0)	mmol m <sup>-3</sup>	0.19 $\pm$ 0.06	0.05 $\pm$ 0.02	0.5 $\pm$ 0.1	0.65 $\pm$ 0.06	0.20 $\pm$ 0.07	T <sub>1</sub> , U <sub>1</sub> < D; T <sub>2</sub> ; U <sub>2</sub> < D
NO <sub>2</sub> <sup>-</sup> (32)	mmol m <sup>-3</sup>	0.47 $\pm$ 0.10	0.65 $\pm$ 0.07	0.8 $\pm$ 0.1	0.50 $\pm$ 0.06	0.45 $\pm$ 0.07	
NH <sub>4</sub> <sup>+</sup> (0)	mmol m <sup>-3</sup>	1.1 $\pm$ 0.2	1.0 $\pm$ 0.1	2.4 $\pm$ 0.4	3.6 $\pm$ 0.7	0.66 $\pm$ 0.08	T <sub>1</sub> , U <sub>1</sub> , U <sub>2</sub> < D
NH <sub>4</sub> <sup>+</sup> (32)	mmol m <sup>-3</sup>	2.0 $\pm$ 0.3	2.8 $\pm$ 0.3	2.5 $\pm$ 0.4	2.1 $\pm$ 0.4	2.2 $\pm$ 0.5	
PO <sub>4</sub> <sup>3-</sup> (0)	mmol m <sup>-3</sup>	0.25 $\pm$ 0.03	0.22 $\pm$ 0.02	0.57 $\pm$ 0.07	0.67 $\pm$ 0.05	0.14 $\pm$ 0.02	U <sub>1</sub> , U <sub>2</sub> , T <sub>1</sub> < D, T <sub>2</sub>
PO <sub>4</sub> <sup>3-</sup> (32)	mmol m <sup>-3</sup>	0.45 $\pm$ 0.05	0.78 $\pm$ 0.04	0.89 $\pm$ 0.06	0.61 $\pm$ 0.04	0.57 $\pm$ 0.06	D, T <sub>1</sub> , U <sub>2</sub> < T <sub>2</sub> ; T <sub>1</sub> < U <sub>1</sub>
Si(0)	mmol m <sup>-3</sup>	2.5 $\pm$ 0.6	0.5 $\pm$ 0.1	4.6 $\pm$ 0.9	9.0 $\pm$ 0.8	0.8 $\pm$ 0.4	U <sub>1</sub> , U <sub>2</sub> < D, T <sub>2</sub> ; T <sub>1</sub> < D
Si(32)	mmol m <sup>-3</sup>	3.4 $\pm$ 0.6	5.6 $\pm$ 0.5	8.0 $\pm$ 0.8	5.1 $\pm$ 0.6	3.2 $\pm$ 0.7	U <sub>1</sub> , U <sub>2</sub> < T <sub>2</sub>
∫ dzNO <sub>3</sub> <sup>-</sup>	mmol m <sup>-2</sup>	130 $\pm$ 20	200 $\pm$ 20	350 $\pm$ 30	330 $\pm$ 20	210 $\pm$ 20	T <sub>1</sub> , U <sub>1</sub> < D, T <sub>2</sub> ; U <sub>2</sub> < T <sub>2</sub>
Z <sub>Chl a</sub>	m	18 $\pm$ 4	14 $\pm$ 2	20 $\pm$ 6	17 $\pm$ 5	8 $\pm$ 3	
∫ dzChl a	mg m <sup>-2</sup>	50 $\pm$ 10	71 $\pm$ 6	31 $\pm$ 6	20 $\pm$ 2	60 $\pm$ 10	D < T <sub>1</sub> , U <sub>1</sub> , U <sub>2</sub> ; T <sub>2</sub> < U <sub>1</sub>
Chl a <sub>0</sub>	mg m <sup>-3</sup>	1.3 $\pm$ 0.3	1.4 $\pm$ 0.3	2.0 $\pm$ 0.8	0.6 $\pm$ 0.1	4 $\pm$ 1	D, T <sub>1</sub> , U <sub>1</sub> < U <sub>2</sub>
Chl a <sub>10</sub>	mg m <sup>-3</sup>	2.2 $\pm$ 0.6	3.8 $\pm$ 0.7	1.3 $\pm$ 0.4	0.6 $\pm$ 0.1	3.0 $\pm$ 0.7	D, T <sub>2</sub> < U <sub>1</sub>
PP <sub>0</sub>	mg m <sup>-3</sup> d <sup>-1</sup>	60 $\pm$ 20	110 $\pm$ 20	110 $\pm$ 50	27 $\pm$ 9	350 $\pm$ 100	D, T <sub>1</sub> , T <sub>2</sub> , U <sub>1</sub> < U <sub>2</sub>
PP <sub>10</sub>	mg m <sup>-3</sup> d <sup>-1</sup>	160 $\pm$ 50	260 $\pm$ 50	60 $\pm$ 20	18 $\pm$ 7	160 $\pm$ 40	D, T <sub>2</sub> < U <sub>1</sub>
μ <sub>0</sub>	d <sup>-1</sup>	0.8 $\pm$ 0.2	1.4 $\pm$ 0.2	0.86 $\pm$ 0.10	1.1 $\pm$ 0.2	1.1 $\pm$ 0.1	
μ <sub>10</sub>	d <sup>-1</sup>	1.4 $\pm$ 0.2	1.0 $\pm$ 0.1	0.72 $\pm$ 0.08	0.7 $\pm$ 0.2	0.8 $\pm$ 0.2	D, T <sub>2</sub> < T <sub>1</sub>

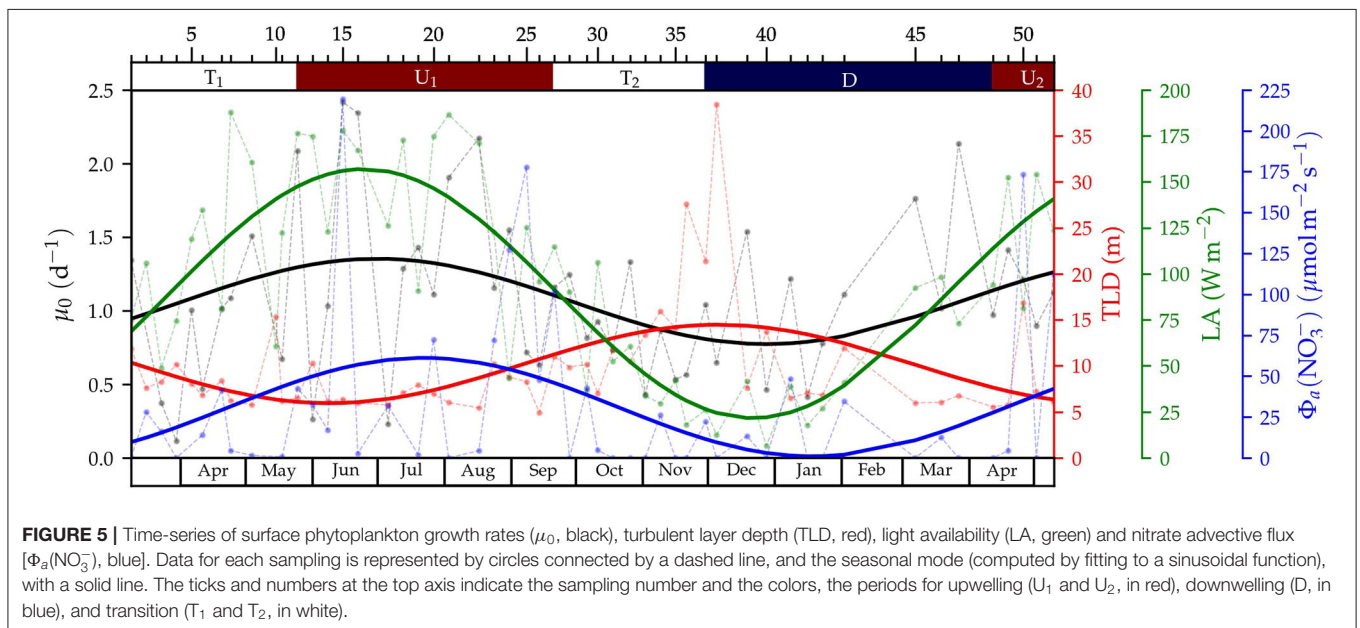
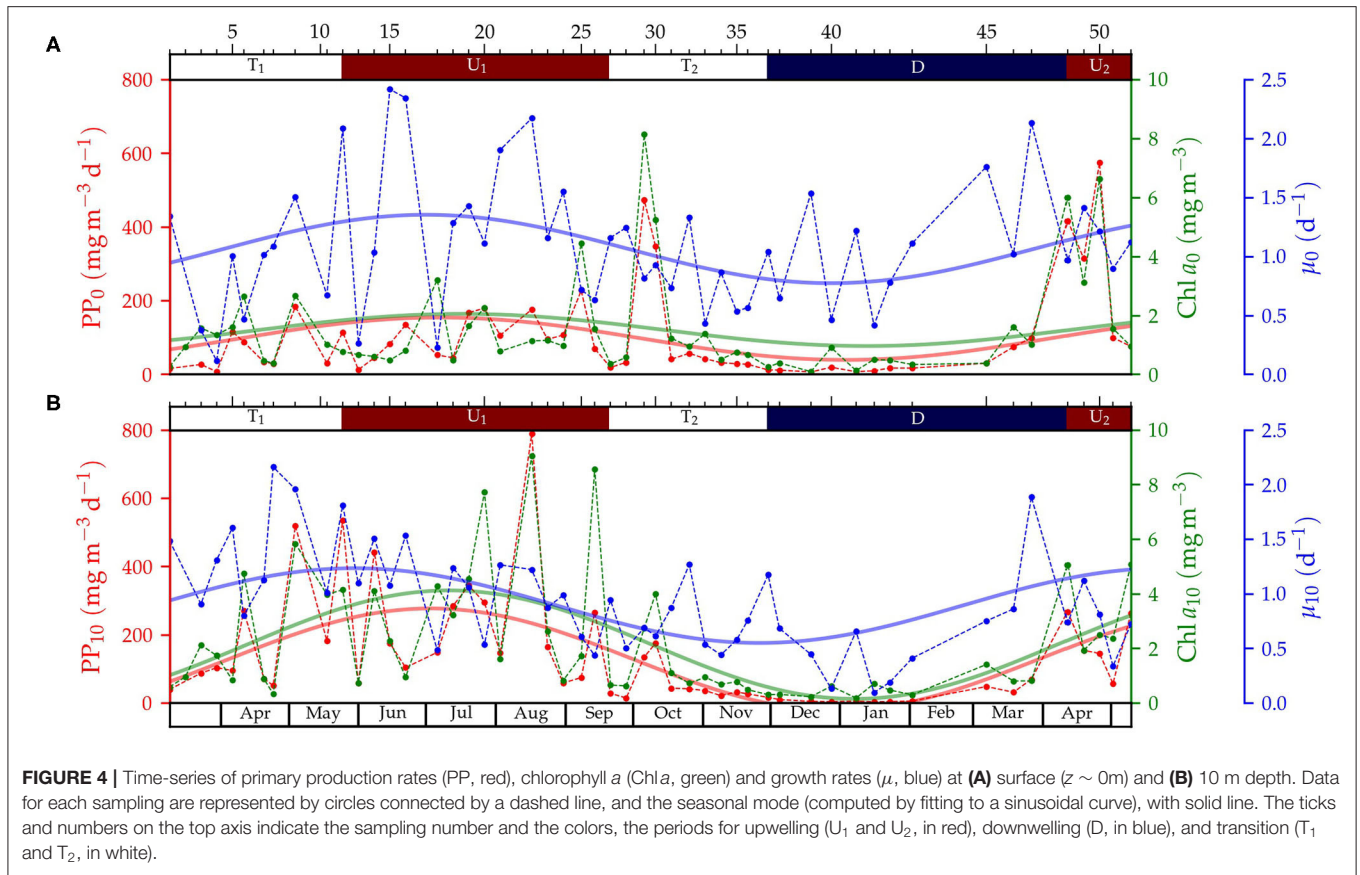
The depth-average for 10–35 m (n = 25) is shown for ε, N<sup>2</sup>, and K. The integrated Chl a (∫ dzChl a, n ~ 40) and the depth of Chl a maximum (Z<sub>Chl a</sub>) in water column were computed from the fluorescence measured with the microstructure turbulence profiler. Also the integrated nitrate concentration (∫ dzNO<sub>3</sub><sup>-</sup>, n ~ 8) was computed. The Tukey's range test was applied to discriminating differences between periods. n indicates the number of points used in each average.

during U<sub>2</sub>) than the transitional T<sub>1</sub> and T<sub>2</sub> and the downwelling period (18  $\pm$  4, 20  $\pm$  3, and 17  $\pm$  5 m, respectively). Higher values of depth-integrated Chl a were measured for the spring-summer upwelling U<sub>1</sub> (71  $\pm$  6 mg m<sup>-2</sup>) and U<sub>2</sub> (60  $\pm$  10 mg m<sup>-2</sup>) periods, whereas lower values were observed during winter downwelling D (20  $\pm$  2 mg m<sup>-2</sup>).

The temporal variability of Chl a concentration, primary production rates and phytoplankton growth rates determined at the surface and 10 m depth from water samples collected from Niskin bottles are shown in **Figure 4**. All these variables exhibited a distinct seasonal variability, which allowed fitting the data to a sinusoidal curve to highlight the seasonal cycle. The amplitude of the seasonal variability for Chl a and primary production was larger at 10 m. In agreement with the chlorophyll-derived fluorescence data from the microstructure profiler, maximum values of extracted Chl a and primary production were measured

during spring-summer upwelling, whereas minimum values were obtained mainly during winter downwelling. On average, Chl a and primary production were lower at the surface than at 10 m depth during the spring transition T<sub>1</sub> and spring-summer upwelling U<sub>1</sub>, whereas the opposite pattern was found during the fall transition T<sub>2</sub>, the winter downwelling and the spring upwelling U<sub>2</sub>.

As the result of the observed variability, phytoplankton growth rates were in general higher at the surface than at 10 meters depth. On average, surface rates were higher during spring-summer upwelling U<sub>1</sub> (1.4  $\pm$  0.2 d<sup>-1</sup>), downwelling (1.1  $\pm$  0.2 d<sup>-1</sup>) and spring upwelling U<sub>2</sub> (1.1  $\pm$  0.1 d<sup>-1</sup>), whereas lower rates were computed during transitional periods T<sub>1</sub> (0.8  $\pm$  0.2 d<sup>-1</sup>) and T<sub>2</sub> (0.9  $\pm$  0.1 d<sup>-1</sup>). At 10 m, growth rates were higher during the spring transitional period T<sub>1</sub> (1.4  $\pm$  0.2 d<sup>-1</sup>) and spring-summer upwelling U<sub>1</sub> (1.0  $\pm$  0.1 d<sup>-1</sup>), whereas



lower values were computed for the transitional  $T_2$  ( $0.72 \pm 0.08 \text{ d}^{-1}$ ) and downwelling period ( $0.7 \pm 0.2 \text{ d}^{-1}$ ). Since higher phytoplankton growth rates were estimated at the surface layer

and a similar seasonal pattern was observed at the two sampling depths, we focus on surface rates to investigate the relationship between phytoplankton growth and mixing.

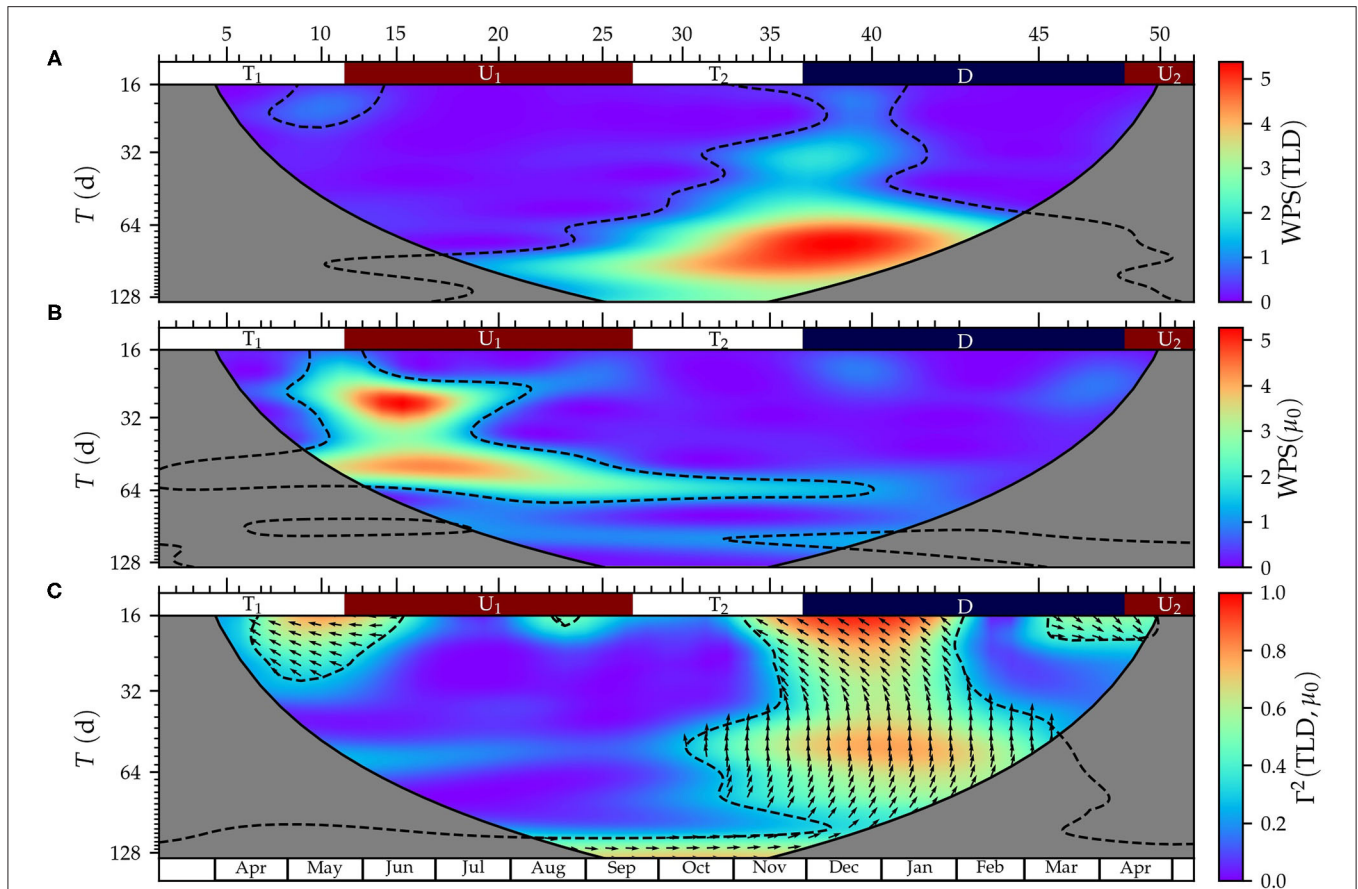


**FIGURE 6** | Wavelet analysis of turbulent layer depth (TLD) and surface phytoplankton growth rates ( $\mu_0$ ). **(A)** Wavelet power spectrum (WPS) of TLD, **(B)** WPS of  $\mu_0$ , and **(C)** wavelet coherence ( $\Gamma^2$ ) and phase difference ( $\delta\phi$ ) between TLD and  $\mu_0$ . The solid black line indicates the cone of influence inside which the edge effects have no influence. The black dashed lines denote the 0.05 significance regions. The arrows indicate  $\delta\phi$  measured with respect to the horizontal axis in the anti-clockwise direction; e.g.,  $\rightarrow$  for  $\delta\phi = 0^\circ$  and  $\uparrow$  for  $\delta\phi = 90^\circ$ . For simplicity, arrows are only plotted inside the regions where significance was higher than 0.05 and only one arrow is plotted every eight period-points. The ticks and numbers at the top axis indicate the sampling number and the colors, the periods for upwelling ( $U_1$  and  $U_2$ , in red), downwelling (D, in blue), and transition ( $T_1$  and  $T_2$ , in white).

### 3.4. Relationship Between Turbulent Mixing and Phytoplankton Growth

We first investigated the relationship between turbulent mixing and surface phytoplankton growth rate over seasonal scales by plotting the variability of the TLD and phytoplankton growth in **Figure 5**. The annual mode, computed for both variables by fitting the observations to a sinusoidal curve, showed that in general maximum growth rates coincided with shallow turbulent layers, whereas minimum values corresponded to deep turbulent layers. Similarly, high phytoplankton growth was coincident with periods of high values of the light and nitrate availability indices, and vice versa.

In addition to the seasonal mode described above, **Figure 5** evidenced the existence of short-term variability both in TLD and phytoplankton growth. In fact, 44 and 60% of the variance of TLD and surface growth rates, respectively, were distributed in periods shorter than 128 d. The wavelet analysis, used to investigate this shorter-term variability (**Figure 6**), showed that TLD variance was larger during the fall transition  $T_2$  and winter downwelling through all the periods with maxima at 34 and 91

days (**Figure 6A**). The variance of surface growth rates displayed two main components extending mostly during the spring-summer upwelling  $U_1$  centered at 26 and 56 days (**Figure 6B**). Growth rates at 10 m (**Supplementary Figure 2A**) exhibited variance maxima during the spring transition  $T_1$  (centered at 25 days), and during the fall transition  $T_2$  and winter downwelling (109 days period).

The relationship between the variance in TLD and surface phytoplankton growth rates was investigated via the coherence ( $\Gamma^2$ ) computed using the wavelet analysis (**Figure 6C**). Also, the phase difference ( $\delta\phi$ ) between both signals was calculated to characterize the delay between the two time-series. The variables are in phase ( $\delta\phi = 0^\circ$ ) when their maxima coincide in time, whereas they are in phase opposition ( $\delta\phi = 180^\circ$ ) when the maximum of one variable coincides with the minimum of the other, and vice versa. TLD and surface growth rates showed significant coherence during the end of the spring transitional  $T_1$  and the beginning of the spring-summer upwelling  $U_1$  (~16–30 d period) and from the end of the fall transitional period  $T_2$  to the middle of the winter downwelling (~16–90 d periods).

The highest coherence ( $\Gamma^2 > 0.8$ ) occurred for periods  $\sim 16$ – $20$  d, for which the averaged phase difference was  $145 \pm 4^\circ$ . The coherence between TLD and growth rates at 10 m depth (**Supplementary Figure 2B**) was significant during the end of the spring transitional  $T_1$  and the beginning of the spring-summer upwelling  $U_1$  ( $\sim 16$ – $56$  d period) and from the fall transitional period  $T_2$  to the spring upwelling  $U_2$  with maximum values at  $\sim 16$  and  $\sim 35$  d.

## 4. DISCUSSION

As far as we know this study represents the first attempt to investigate the relationship between mixing and phytoplankton growth, by using coincident observations of microstructure turbulence and phytoplankton growth, in a coastal upwelling system. In general, higher turbulent mixing was observed during fall-winter transitional and downwelling periods, whereas weaker mixing corresponded to spring-summer transition and upwelling. However, this pattern was mainly driven by the enhanced turbulent diffusivity quantified during two samplings (36 and 38 sampled on 21 November 2017 and 5 December 2017, respectively). This increase in diffusivity was mainly due to a decrease in the buoyancy frequency, as the consequence of the weak vertical gradient observed in both temperature and salinity. According to the analysis of hydrographic and current velocity data, these two samplings were under the influence of fall upwelling conditions. Although this system is characterized by predominant upwelling conditions during the spring and summer (Fraga, 1981), previous studies described the existence of an important short-term variability in wind conditions, which generates a succession of upwelling-downwelling episodes in periods of 15 days (Álvarez-Salgado et al., 1993; Nogueira et al., 1997; Figueiras et al., 2002). Recently, using direct observations of currents, the mean duration of these upwelling-downwelling episodes has been estimated in  $\sim 3$  days (Gilcoto et al., 2017). The vertical homogenization of the thermohaline conditions, due to the advection of salty oceanic waters inside the Rías, during fall upwelling events erodes the frequent haline stratification driven by increasing precipitation and runoff (Rosón et al., 2008), and enhances mixing.

The seasonality of turbulent mixing in the upper ocean, both in coastal and open-ocean regions, remains poorly assessed due to the limited number of microstructure observations spanning entire annual cycles, such that the limited present knowledge derived mostly from indirect methods (Whalen et al., 2012; Warner et al., 2016; Inoue et al., 2017; Evans et al., 2018; Thakur et al., 2019; Cherian et al., 2020). Previous studies carried out in this region provided information about the variability of turbulent diffusivity on short-time scales during specific seasons (Barton et al., 2016; Villamaña et al., 2017; Fernández-Castro et al., 2018; Broullón et al., 2020) or along seasonal scales with coarser temporal resolution (Cermeño et al., 2016; Moreira-Coello et al., 2017).

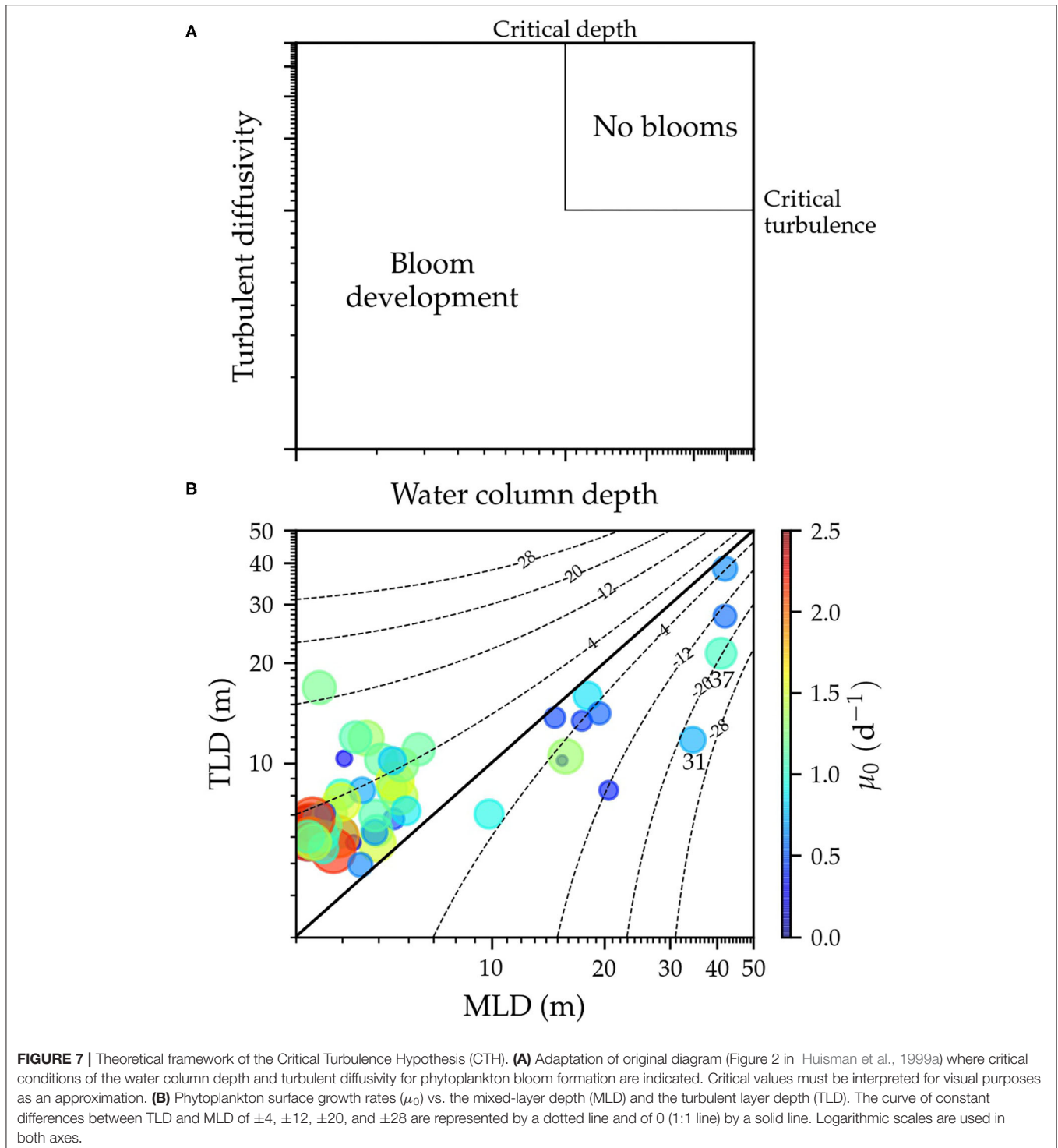
Our results show that surface growth rates, which ranged from  $0.11$  to  $2.42$   $\text{d}^{-1}$  ( $0.008$ – $0.226$   $\text{h}^{-1}$ ), were in general higher

during spring-summer transitional and upwelling periods, and minimum during fall-winter transitional and downwelling. These values are consistent with previous estimates determined for this system, by using a similar methodology, but with coarser temporal resolution. An early study carried out in the Ría de Arousa during an upwelling event (Hanson et al., 1986), reported depth-averaged phytoplankton growth rates ranging from  $< 0.1$  to  $1.89$   $\text{d}^{-1}$  (from  $< 0.004$  to  $0.0788$   $\text{h}^{-1}$ ). Cermeño et al. (2016) estimated slightly lower phytoplankton growth rates at the same station in the Ría de Vigo ( $\sim 0.004$ – $0.114$   $\text{h}^{-1}$ ). Our data, derived from short (2 h) incubations experiments, are also consistent with apparent phytoplankton growth rates estimated from the dilution technique which ranged from  $0.31$  to  $1.75$   $\text{d}^{-1}$  (Teixeira and Figueiras, 2009). However, maybe due to aliasing of short-term variability in their coarser observations, previous studies in the region did not report a clear seasonal cycle in phytoplankton growth rates. Seasonal trends in phytoplankton growth, consistent with our findings, have been described in several studies carried out in contrasting regions, mainly by using the dilution technique (Kim et al., 2007; Gutiérrez-Rodríguez et al., 2011; Lawrence and Menden-Deuer, 2012; Anderson and Harvey, 2019).

The temporal coverage and resolution of our study allowed interpreting our results within the conceptual framework of the Critical Turbulence Hypothesis (CTH, Huisman et al., 1999a,b, **Figure 7A**). According to the CTH, positive net phytoplankton growth will occur when (1) the water column depth is shallower than the critical depth, which is consistent with the Critical Depth Hypothesis (CDH, Sverdrup, 1953), or (2) when turbulent diffusivity in a mixed water column is lower than a critical value, which causes the timescale for phytoplankton growth to be less than the cell's residence time in the portion of the water column where net growth can be achieved. In this case, the depth of the turbulent layer would be shallower than the mixed layer depth.

Huisman et al. (1999a) described these two distinct and independent mechanisms by using simulations with variable turbulent diffusivity and water column depth. Similar to the CDH, they assumed that phytoplankton growth was only limited by light, and also constant values in time and depth for turbulence diffusivity and the phytoplankton loss term. In order to interpret our results under this theoretical framework, we performed some modifications on the original diagram (**Figure 7A**). First, we used the mixed-layer depth instead of the water column depth, to indicate the depth of the water column where density was relatively vertically homogeneous. Second, we used the turbulent layer depth, instead of turbulent diffusivity, to consider both the magnitude and the vertical structure of turbulent mixing. Finally, we used surface growth rate instead of depth-integrated phytoplankton growth rates to represent phytoplankton growth in the turbulent layer (**Figure 7B**). Consequently, phytoplankton growth was always positive and its variability must be interpreted in relative terms instead of positive or negative growth, as in the original diagram.

In agreement with the first scenario proposed by the CTH, our results showed that higher phytoplankton growth rates were found for periods of shallow turbulent and mixed-layers during spring-summer transitional and upwelling periods, whereas low



values were observed during periods of deep turbulent and mixed-layers (fall-winter transitional and downwelling periods). Unfortunately, our dataset was not suitable to assess the second scenario described by Huisman et al. (1999a), as most observations corresponded to shallow mixed- and turbulent

layers. Only two samplings (31 and 37) showed the mixed-layer to be much deeper ( $\sim 20$  m) than the turbulent layer, suggesting that the mixed-layer was not actively mixing in  $<1$  day. The surface phytoplankton growth rate for sampling 31, 2 days after the passage of Hurricane Ophelia, was relatively low (0.73

$d^{-1}$ ), whereas this rate was slightly higher during sampling 37 ( $1.0 d^{-1}$ ).

Due to the difficulty to quantify turbulence in the field, previous studies using the CTH theoretical framework mainly used hydrographic and atmospheric data to infer mixing conditions in the upper layer, and its relationship with phytoplankton growth in different regions as the North Atlantic (Chiswell, 2011; Chiswell et al., 2013; Mignot et al., 2018), the North West European Shelf (Wihsgott et al., 2019), the southwest Pacific (Chiswell, 2011; Chiswell et al., 2013), the Western Mediterranean Sea (Bernardello et al., 2012; Kessouri et al., 2018), the Chukchi Sea (Lowry et al., 2018), and the Labrador Sea (Marchese et al., 2019). The decrease in turbulence that could explain the TLD being shallower than the MLD (second scenario proposed for the CTH) has been associated with a reduction in air-sea fluxes that generally precedes mixed-layer shoaling at the end of winter (Taylor and Ferrari, 2011) and lowered wind stress (Chiswell, 2011; Chiswell et al., 2013). Moreover, Brody and Lozier (2014) proposed that the mixing-length scale of the largest energy-containing eddies in the upper ocean is a better predictor for bloom initiation than the decrease in mixed-layer depth, the onset of positive heat fluxes, or the decrease in wind strength. They also found that the shift from buoyancy-driven to wind-driven mixing in late winter creates the decrease in mixing length scale, and thus the conditions necessary for blooms to begin (Brody and Lozier, 2015).

Only a limited number of studies have previously used microstructure observations to investigate the relationship between turbulence and phytoplankton activity and composition. Among those, most studies were focused on analyzing the role of mixing and nutrient supply as drivers of phytoplankton community structure (Sharples et al., 2007, 2009; Machado et al., 2014; Villamaña et al., 2017, 2019). As far as we know only two studies have used microturbulence observations to investigate phytoplankton growth under the CTH framework. Huisman et al. (2004) extended the CTH including competition theory, to predict how changes in turbulent mixing affect competition for light between buoyant and sinking phytoplankton species. Consistent with the model prediction, results from a lake experiment showed that changes in turbulent mixing caused a dramatic shift in phytoplankton species composition. In coherence with the CTH, Hopkins et al. (2021) used a relatively short (2 weeks) period of high-frequency (sub-hourly) observations collected from gliders in the Northwest European Shelf to conclude that turbulent mixing, that mediate light availability, was the key process governing phytoplankton growth in spring.

Our study covers a full annual cycle which allows investigating the coupling between turbulent mixing and phytoplankton growth at different temporal scales. Our results show that shallower mixed- and turbulent layers conditions were not enough to ensure phytoplankton growth, as low phytoplankton growth was also found under these circumstances. It is important to note that, instead of following a single phytoplankton bloom over time, our weekly approach involves sampling different blooms at different stages of development. Previous studies in this region have described that the spring-summer and fall

phytoplankton growth seasons are the result of a succession of blooms triggered by the short-term variability in the upwelling regime and runoff water pulses (Nogueira and Figueiras, 2005). This is consistent with observations carried out in the North Atlantic where fluctuations in the winter mixed-layer depth triggered occasional short-live blooms (Mignot et al., 2018). Using a wavelet transform analysis we showed that the coupling between turbulent mixing and phytoplankton growth in this system occurs not only over the seasonal cycle, but also at shorter temporal scales. These results suggest that mixing could act as a control factor on phytoplankton growth over the seasonal cycle, but also being involved in the formation of occasional short-lived phytoplankton blooms.

## 5. CONCLUSIONS

By analyzing a unique dataset combining weekly observations of microstructure turbulence and phytoplankton growth collected in the NW Iberian coastal upwelling we show that coupling between turbulent mixing and phytoplankton growth occurs over the seasonal cycle, but also at shorter temporal scales. In agreement with the Critical Turbulence Hypothesis (Huisman et al., 1999a,b), our results indicate that higher values of phytoplankton growth occurred during spring-summer transitional and upwelling periods, when the depth of the turbulent layer was shallower, whereas the opposite pattern was observed during fall-winter transitional and downwelling periods. However, shallower turbulent layers were not enough to stimulate phytoplankton growth, as low growth rates were observed during the same conditions. Despite our unprecedented sampling effort, we are aware that a significant part of the variability in this system was still not captured, which deterred us from unveiling the mechanisms driving the coupling between mixing and phytoplankton growth rates, specially at short time-scales. Furthermore, longer observations will be needed to discern whether the seasonal patterns described here are characteristic of the study system or determined by the specific investigated sampling period.

The Critical Turbulence Hypothesis assumes that phytoplankton growth is exclusively limited by light and that the phytoplankton loss rate is independent of depth and constant through time. However, mixing conditions in the water column influence light but also nutrient availability for phytoplankton cells. Our results indicate that, in general, higher phytoplankton growth occurs when light but also nitrate availability was higher. Although our study was performed in a nutrient-rich coastal upwelling ecosystem, previous studies in the region have shown that phytoplankton is limited by nitrogen during the summer, or at least it positively responds to its addition (Martínez-García et al., 2010). Moreover, although phytoplankton blooms have traditionally been attributed to changes in “bottom-up” environmental factors controlling phytoplankton division rates, such as light and nutrients (e.g., Hunter-Cevera et al., 2016; Wihsgott et al., 2019), changes in phytoplankton biomass are the result of the interplay between phytoplankton division rates and the sum of all loss terms.

Recent studies using satellite, *in situ* observations and modeling approaches highlighted the relevance of variability in loss rates (Behrenfeld, 2010; Boss and Behrenfeld, 2010; Behrenfeld et al., 2013). The Disturbance Recovery Hypothesis proposed by Behrenfeld and Boss (2014) argues that, contrary to the CDH, bloom initiation takes place in the winter because deep mixing dilutes phytoplankton cell density, thus reducing the encounter rate between predator and prey. It is important to note that our phytoplankton growth estimates, as derived from short carbon uptake experiments, are close to gross rates, and therefore do not reflect the balance between cell division and loss rates. Moreover, the time step we used for the wavelet analysis (8 days) is much longer than the time-scale for phytoplankton growth (~1 day). Future studies combining higher temporal resolution and longer observations, together with modeling approaches will be required in order to discern the mechanisms responsible for the coupling between mixing and phytoplankton growth observed in this system, and to evaluate the role of “bottom-up” and “top-down” control factors.

Despite their small surface extension (1% of the global ocean) eastern boundary upwelling systems account for 5% to the global marine primary production (Carr, 2001) and 20% of global fish catch (Chavez and Messié, 2009). One unresolved question in these regions is the regulation of primary production. Substantial variability in the ratio of nitrate supply to primary production has been described (Messié et al., 2009), indicating that regulators other than nitrate supply must be at play. In agreement with previous studies (Hardman-Mountford et al., 2003; Rossi et al., 2009; Fearon et al., 2020), our results indicate that turbulent mixing may control phytoplankton growth at the different time-scales involved in the physical-biological coupling in these systems.

Anthropogenic global change perturbations have the potential to affect phytoplankton dynamics, including the timing and magnitude of blooms (e.g., Hunter-Cevera et al., 2016; Jena and Narayana Pillai, 2020). Therefore, identifying the mechanisms responsible for the formation of phytoplankton blooms,

including turbulent mixing (Károly et al., 2020), is key to understand the role of the ocean in the present and future climate.

## DATA AVAILABILITY STATEMENT

The original contributions presented in the study are included in the article/**Supplementary Material**, further inquiries can be directed to the corresponding author/s.

## AUTHOR CONTRIBUTIONS

AC, BM-C, and BF-C designed the overall study. PC, EF, AF-L, MG, MP-L, and BM-C carried out the observations and performed experiments in the lab. AC analyzed the dataset. AC, BM-C, and BF-C prepared the manuscript with contributions from all the co-authors. All authors contributed to the article and approved the submitted version.

## FUNDING

This research was supported by grant CTM2016-75451-C2-1-R from the Spanish Ministry of Economy and Competitiveness to BM-C. AC was supported by a predoctoral fellowship for the doctoral formation (BES-2017-080935) from the Spanish Ministry of Economy and Competitiveness.

## ACKNOWLEDGMENTS

We thank the crew of the R/V Kraken and the R/V José María Navaz, and also all the scientists involved in data and water samples collection, for their valuable support during the sampling at sea.

## SUPPLEMENTARY MATERIAL

The Supplementary Material for this article can be found online at: <https://www.frontiersin.org/articles/10.3389/fmars.2021.712342/full#supplementary-material>

## REFERENCES

- Acuña, J. L., López-Alvarez, M., Nogueira, E., and González-Taboada, F. (2010). Diatom flotation at the onset of the spring phytoplankton bloom: an *in situ* experiment. *Mar. Ecol. Prog. Ser.* 400, 115–125. doi: 10.3354/meps08405
- Álvarez-Salgado, X. A., Rosón, G., F. Pérez, F., Figueiras, F., and Ríos, A. (1996). Nitrogen cycling in an estuarine upwelling system, the Ría de Arousa (NW Spain). II. Spatial differences in the short-time-scale evolution of fluxes and net budgets. *Mar. Ecol. Prog. Ser.* 135, 275–288.
- Álvarez-Salgado, X. A., Rosón, G., Pérez, F. F., and Pazos, Y. (1993). Hydrographic variability off the Rías Baixas (NW Spain) during the upwelling season. *J. Geophys. Res.* 98, 14447–14455. doi: 10.1029/93JC00458
- Anderson, S. R., and Harvey, E. L. (2019). Seasonal variability and drivers of microzooplankton grazing and phytoplankton growth in a subtropical estuary. *Front. Mar. Sci.* 6:174. doi: 10.3389/fmars.2019.00174
- Arteaga, L., Boss, E., Behrenfeld, M., Westberry, T., and Sarmiento, J. (2020). Seasonal modulation of phytoplankton biomass in the southern ocean. *Nat. Commun.* 11:5364. doi: 10.1038/s41467-020-19157-2
- Backhaus, J., Wehde, H., Hegseth, E., and Kämpf, J. (1999). “Phyto-convection”: the role of oceanic convection in primary production. *Mar. Ecol. Prog. Ser.* 189, 77–92. doi: 10.3354/meps189077
- Bakun, A. (1973). *Coastal Upwelling Indices, West Coast of North America, 1946-71*. Technical report, United States, Department of Commerce, National Oceanic and Atmospheric Administration, National Marine Fisheries Service.
- Barton, E. D., Torres, R., Figueiras, F. G., Gilcoto, M., and Largier, J. (2016). Surface water subduction during a downwelling event in a semienclosed bay. *J. Geophys. Res.* 121, 7088–7107. doi: 10.1002/2016JC011950
- Behrenfeld, M. J. (2010). Abandoning Sverdrup’s Critical Depth Hypothesis on phytoplankton blooms. *Ecology* 91, 977–989. doi: 10.1890/09-1207.1
- Behrenfeld, M. J., and Boss, E. S. (2014). Resurrecting the ecological underpinnings of ocean plankton blooms. *Annu. Rev. Mar. Sci.* 6, 167–194. doi: 10.1146/annurev-marine-052913-021325
- Behrenfeld, M. J., Doney, S. C., Lima, I., Boss, E. S., and Siegel, D. A. (2013). Annual cycles of ecological disturbance and recovery underlying the subarctic Atlantic spring plankton bloom. *Glob. Biogeochem. Cycles* 27, 526–540. doi: 10.1002/gbc.20050

- Bernardello, R., Cardoso, J. G., Bahamon, N., Donis, D., Marinov, I., and Cruzado, A. (2012). Factors controlling interannual variability of vertical organic matter export and phytoplankton bloom dynamics—a numerical case-study for the NW Mediterranean Sea. *Biogeosciences* 9, 4233–4245. doi: 10.5194/bg-9-4233-2012
- Boss, E., and Behrenfeld, M. (2010). *In situ* evaluation of the initiation of the North Atlantic phytoplankton bloom. *Geophys. Res. Lett.* 37, 1–5. doi: 10.1029/2010GL044174
- Brainerd, K. E., and Gregg, M. C. (1995). Surface mixed and mixing layer depths. *Deep Sea Res. Part I Oceanogr. Res. Pap.* 42, 1521–1543.
- Brody, S. R., and Lozier, M. S. (2014). Changes in dominant mixing length scales drive phytoplankton bloom initiation in the subpolar North Atlantic. *Geophys. Res. Lett.* 41, 3197–3203. doi: 10.1002/2014GL059707
- Brody, S. R., and Lozier, M. S. (2015). Characterizing upper-ocean mixing and its effect on the spring phytoplankton bloom with *in situ* data. *ICES J. Mar. Sci.* 72, 1961–1970. doi: 10.1093/icesjms/fsv006
- Brody, S. R., Lozier, M. S., and Dunne, J. P. (2013). A comparison of methods to determine phytoplankton bloom initiation. *J. Geophys. Res.* 118, 2345–2357. doi: 10.1002/jgrc.20167
- Broullón, E., López-Mozos, M., Reguera, B., Chouciño, P., Dolores Doval, M., Fernández-Castro, B., et al. (2020). Thin layers of phytoplankton and harmful algae events in a coastal upwelling system. *Prog. Oceanogr.* 189:102449. doi: 10.1016/j.pocean.2020.102449
- Carr, M.-E. (2001). Estimation of potential productivity in eastern boundary currents using remote sensing. *Deep Sea Res. Part II Top. Stud. Oceanogr.* 49, 59–80. doi: 10.1016/S0967-0645(01)00094-7
- Cazelles, B., Cazelles, K., and Chavez, M. (2014). Wavelet analysis in ecology and epidemiology: impact of statistical tests. *J. R. Soc. Interface* 11:20130585. doi: 10.1098/rsif.2013.0585
- Cazelles, B., Chavez, M., Berteaux, D., Ménard, F., Vik, J. O., Jenouvrier, S., and Stenseth, N. C. (2008). Wavelet analysis of ecological time series. *Oecologia* 156, 287–304. doi: 10.1007/s00442-008-0993-2
- Cazelles, B., and Stone, L. (2003). Detection of imperfect population synchrony in an uncertain world. *J. Anim. Ecol.* 72, 953–968. doi: 10.1046/j.1365-2656.2003.00763.x
- Cermeño, P., Chouciño, P., Fernández-Castro, B., Figueiras, F. G., Marañón, E., Marrasé, C., et al. (2016). Marine primary productivity is driven by a selection effect. *Front. Mar. Sci.* 3:173. doi: 10.3389/fmars.2016.00173
- Cermeño, P., Marañón, E., Pérez, V., Serret, P., Fernández, E., and Castro, C. G. (2006). Phytoplankton size structure and primary production in a highly dynamic coastal ecosystem (Ría de Vigo, NW-Spain): seasonal and short-time scale variability. *Estuar. Coast. Shelf Sci.* 67, 251–266. doi: 10.1016/j.ecss.2005.11.027
- Cermeño, P., Marañón, E., Rodríguez, J., and Fernández, E. (2005). Large-sized phytoplankton sustain higher carbon-specific photosynthesis than smaller cells in a coastal eutrophic ecosystem. *Mar. Ecol. Prog. Ser.* 297, 51–60. doi: 10.3354/meps297051
- Chavez, F. P., and Messié, M. (2009). A comparison of eastern boundary upwelling ecosystems. *Prog. Oceanogr.* 83, 80–96. doi: 10.1016/j.pocean.2009.07.032
- Cherian, D. A., Shroyer, E. L., Wijesekera, H. W., and Moum, J. N. (2020). The seasonal cycle of upper-ocean mixing at 8°N in the Bay of Bengal. *J. Phys. Oceanogr.* 50, 323–342. doi: 10.1175/JPO-D-19-0114.1
- Chiswell, S. M. (2011). Annual cycles and spring blooms in phytoplankton: don't abandon Sverdrup completely. *Mar. Ecol. Prog. Ser.* 443, 39–50. doi: 10.3354/meps09453
- Chiswell, S. M., Bradford-Grieve, J., Hadfield, M. G., and Kennan, S. C. (2013). Climatology of surface chlorophyll a, autumn-winter and spring blooms in the southwest Pacific Ocean. *J. Geophys. Res.* 118, 1003–1018. doi: 10.1002/jgrc.20088
- Chiswell, S. M., Calil, P. H., and Boyd, P. W. (2015). Spring blooms and annual cycles of phytoplankton: a unified perspective. *J. Plankton Res.* 37, 500–508. doi: 10.1093/plankt/fbv021
- Ellertsen, H. C. (1993). Spring blooms and stratification. *Nature* 363:24. doi: 10.1038/363024a0
- Evans, D. G., Lucas, N. S., Hemsley, V., Frajka-Williams, E., Naveira Garabato, A. C., Martin, A., et al. (2018). Annual cycle of turbulent dissipation estimated from seaglidars. *Geophys. Res. Lett.* 45, 10,560–10,569. doi: 10.1029/2018GL079966
- Fearon, G., Herbette, S., Veitch, J., Cambon, G., Lucas, A. J., Lemarié, F., et al. (2020). Enhanced vertical mixing in coastal upwelling systems driven by diurnal-inertial resonance: numerical experiments. *J. Geophys. Res.* 125, 1–23. doi: 10.1029/2020JC016208
- Fernández, E., Álvarez-Salgado, X. Á., Beiras, R., Ovejero, A., and Martínez, G. (2016). Coexistence of urban uses and shellfish production in an upwelling-driven, highly productive marine environment: the case of the ría de vigo (Galicia, Spain). *Region. Stud. Mar. Sci.* 8, 362–370. doi: 10.1016/j.rsmas.2016.04.002
- Fernández-Castro, B., Gilcoto, M., Naveira-Garabato, A. C., Villamaña, M., Graña, R., and Mouriño-Carballido, B. (2018). Modulation of the semidiurnal cycle of turbulent dissipation by wind-driven upwelling in a coastal embayment. *J. Geophys. Res.* 123, 4034–4054. doi: 10.1002/2017jc013582
- Field, C., Behrenfeld, M., Randerson, J., and Falkowski, P. (1998). Primary production of the biosphere: Integrating terrestrial and oceanic components. *Science* 281, 237–240. doi: 10.1126/science.281.5374.237
- Figueiras, F. G., Labarta, U., and Reiriz, M. J. F. (2002). *Coastal Upwelling, Primary Production and Mussel Growth in the Rias Baixas of Galicia*. Dordrecht: Springer Netherlands.
- Fraga, F. (1981). Upwelling off the Galician coast, northwest Spain. *Estuar. Sci.* 1, 176–182. doi: 10.1029/CO001p0176
- Franks, P. J. S. (2015). Has Sverdrup's critical depth hypothesis been tested? Mixed layers vs. turbulent layers. *ICES J. Mar. Sci.* 72, 1897–1907. doi: 10.1093/icesjms/fsu175
- Fréon, P., Barange, M., and Aristegui, J. (2009). Eastern boundary upwelling ecosystems: integrative and comparative approaches. *Prog. Oceanogr.* 83, 1–14. doi: 10.1016/j.pocean.2009.08.001
- Gilcoto, M., Largier, J. L., Barton, E. D., Piedracoba, S., Torres, R., Graña, R., et al. (2017). Rapid response to coastal upwelling in a semienclosed bay. *Geophys. Res. Lett.* 44, 2388–2397. doi: 10.1002/2016GL072416
- Godin, G. (1972). *The Analysis of Tides*. Toronto, ON; Buffalo, NY: University of Toronto Press.
- Gomez-Gesteira, M., Moreira, C., Alvarez, I., and de Castro, M. (2006). Ekman transport along the Galician coast (Northwest Spain) calculated from forecasted winds. *J. Geophys. Res.* 111. doi: 10.1029/2005JC003331
- Gregg, M. C., D'Asaro, E. A., Riley, J. J., and Kunze, E. (2018). Mixing efficiency in the ocean. *Annu. Rev. Mar. Sci.* 10, 443–473. doi: 10.1146/annurev-marine-121916-063643
- Gutiérrez-Rodríguez, A., Latasa, M., Scharek, R., Massana, R., Vila, G., and Gasol, J. M. (2011). Growth and grazing rate dynamics of major phytoplankton groups in an oligotrophic coastal site. *Estuar. Coast. Shelf Sci.* 95, 77–87. doi: 10.1016/j.ecss.2011.08.008
- Hansen, H. P., and Koroleff, F. (2007). "Determination of nutrients," in *Methods of Seawater Analysis* eds K. Grasshoff, K. Kremling and M. Ehrhardt (Weinheim: Wiley-VCH Verlag GmbH), 159–228.
- Hanson, R. B., Alvarez-Ossorio, M. T., Cal, R., Campos, M. J., Roman, M., Santiago, G., et al. (1986). Plankton response following a spring upwelling event in the Ría de Arosa, Spain. *Mar. Ecol. -Prog. Ser.* 32, 101–113.
- Hardman-Mountford, N., Richardson, A., Agenbag, J., Hagen, E., Nykjaer, L., Shillington, F., et al. (2003). Ocean climate of the south east Atlantic observed from satellite data and wind models. *Prog. Oceanogr.* 59, 181–221. doi: 10.1016/j.pocean.2003.10.001
- Hopkins, J. E., Palmer, M. R., Poulton, A. J., Hickman, A. E., and Sharples, J. (2021). Control of a phytoplankton bloom by wind-driven vertical mixing and light availability. *Limnol. Oceanogr.* 66, 1926–1949. doi: 10.1002/lno.11734
- Huisman, J., Sharples, J., Stroom, J. M., Visser, P. M., Kardinaal, W. E. A., Verspagen, J. M. H., et al. (2004). Changes in turbulent mixing shift competition for light between phytoplankton species. *Ecology* 85, 2960–2970. doi: 10.1890/03-0763
- Huisman, J., van Oostveen, P., and Weissing, F. (1999a). Critical depth and critical turbulence: two different mechanisms for the development of phytoplankton blooms. *Limnol. Oceanogr.* 44, 1781–1787.
- Huisman, J., van Oostveen, P., and Weissing, F. J. (1999b). Species dynamics in phytoplankton blooms: incomplete mixing and competition for light. *Am. Nat.* 154, 46–68.
- Hunter-Cevera, K. R., Neubert, M. G., Olson, R. J., Solow, A. R., Shalapyonok, A., and Sosik, H. M. (2016). Physiological and ecological drivers of

- early spring blooms of a coastal phytoplankton. *Science* 354, 326–329. doi: 10.1126/science.aaf8536
- Inoue, R., Watanabe, M., and Osafune, S. (2017). Wind-induced mixing in the North Pacific. *J. Phys. Oceanogr.* 47, 1587–1603. doi: 10.1175/JPO-D-16-0218.1
- Jena, B., and Narayana Pillai, A. (2020). Satellite observations of unprecedented phytoplankton blooms in the Maud rise Polynya, southern ocean. *Cryosphere* 14, 1385–1398. doi: 10.5194/tc-14-1385-2020
- Károly, G., Prokaj, R. D., Scheuring, I., and Tél, T. (2020). Climate change in a conceptual atmosphere-phytoplankton model. *Earth Syst. Dyn.* 11, 603–615. doi: 10.5194/esd-11-603-2020
- Kessouri, F., Ulses, C., Estournel, C., Marsaleix, P., D'Ortenzio, F., Severin, T., et al. (2018). Vertical mixing effects on phytoplankton dynamics and organic carbon export in the Western Mediterranean Sea. *J. Geophys. Res.* 123, 1647–1669. doi: 10.1002/2016JC012669
- Kim, S., Park, M. G., Moon, C., Shin, K., and Chang, M. (2007). Seasonal variations in phytoplankton growth and microzooplankton grazing in a temperate coastal embayment, Korea. *Estuar. Coast. Shelf Sci.* 71, 159–169. doi: 10.1016/j.ecss.2006.07.011
- Körtzinger, A., Send, U., Lampitt, R. S., Hartman, S., Wallace, D. W. R., Karstensen, J., et al. (2008). The seasonal pCO<sub>2</sub> cycle at 49°N/16.5°W in the Northeastern Atlantic Ocean and what it tells us about biological productivity. *J. Geophys. Res.* 113, 1–15. doi: 10.1029/2007JC004347
- Lawrence, C., and Menden-Deuer, S. (2012). Drivers of protistan grazing pressure: seasonal signals of plankton community composition and environmental conditions. *Mar. Ecol. Prog. Ser.* 459, 39–52. doi: 10.3354/meps09771
- Liu, P. C. (1994). “Wavelet spectrum analysis and ocean wind waves,” in *Wavelets in Geophysics, Vol. 4 of Wavelet Analysis and Its Applications*, eds E. Foufoula-Georgiou and P. Kumar (San Diego, CA: Academic Press), 151–166. doi: 10.1016/B978-0-08-052087-2.50012-8
- Lowry, K. E., Pickart, R. S., Selz, V., Mills, M. M., Pacini, A., Lewis, K. M., et al. (2018). Under-ice phytoplankton blooms inhibited by spring convective mixing in refreezing leads. *J. Geophys. Res.* 123, 90–109. doi: 10.1002/2016JC012575
- Machado, D. A., Marti, C. L., and Imberger, J. (2014). Influence of microscale turbulence on the phytoplankton of a temperate coastal embayment, Western Australia. *Estuar. Coast. Shelf Sci.* 145, 80–95. doi: 10.1016/j.ecss.2014.04.018
- Marchese, C., Castro de la Guardia, L., Myers, P. G., and Bélanger, S. (2019). Regional differences and inter-annual variability in the timing of surface phytoplankton blooms in the Labrador Sea. *Ecol. Indic.* 96, 81–90. doi: 10.1016/j.ecolind.2018.08.053
- Margalef, R. (1978). Life-forms of phytoplankton as survival alternatives in an unstable environment. *Oceanol. Acta* 1, 493–509.
- Martínez-García, S., Fernández, E., Álvarez-Salgado, X. A., González, J., Lonborg, C., Marañón, E., et al. (2010). Differential responses of phytoplankton and heterotrophic bacteria to organic and inorganic nutrient additions in coastal waters off the NW Iberian Peninsula. *Mar. Ecol. Prog. Ser.* 416, 17–33. doi: 10.3354/meps08776
- Menzel, D. W., and Ryther, J. H. (1961). Annual variations in primary production of the Sargasso sea off Bermuda. *Deep Sea Res.* 7, 282–288. doi: 10.1016/0146-6313(61)90046-6
- Messié, M., and Chavez, F. P. (2015). Seasonal regulation of primary production in eastern boundary upwelling systems. *Prog. Oceanogr.* 134, 1–18. doi: 10.1016/j.pocean.2014.10.011
- Messié, M., Ledesma, J., Kolber, D. D., Michisaki, R. P., Foley, D. G., and Chavez, F. P. (2009). Potential new production estimates in four eastern boundary upwelling ecosystems. *Prog. Oceanogr.* 83, 151–158. doi: 10.1016/j.pocean.2009.07.018
- Mignot, A., Ferrari, R., and Claustre, H. (2018). Floats with bio-optical sensors reveal what processes trigger the North Atlantic bloom. *Nat. Commun.* 9, 1–9. doi: 10.1038/s41467-017-02143-6
- Moncoiffe, G., Álvarez-Salgado, X. A., Figueiras, F., and Savidge, G. (2000). Seasonal and short-time-scale dynamics of microplankton community production and respiration in an inshore upwelling system. *Mar. Ecol. Prog. Ser.* 196, 111–126. doi: 10.3354/meps196111
- Moreira-Coello, V., Mouriño-Carballido, B., Marañón, E., Fernández-Carrera, A., Bode, A., and Varela, M. M. (2017). Biological N<sub>2</sub> fixation in the upwelling region off NW Iberia: magnitude, relevance, and players. *Front. Mar. Sci.* 4:303. doi: 10.3389/fmars.2017.00303
- Morel, A. (1988). Optical modeling of the upper ocean in relation to its biogenous matter content (Case I Waters). *J. Geophys. Res.* 93, 10749–10768.
- Nelson, D. M., and Smith, W. (1991). Sverdrup revisited: critical depths, maximum chlorophyll levels, and the control of Southern Ocean productivity by the irradiance-mixing regime. *Limnol. Oceanogr.* 36, 1650–1661. doi: 10.4319/lo.1991.36.8.1650
- Nogueira, E., and Figueiras, F. (2005). The microplankton succession in the Ría de Vigo revisited: species assemblages and the role of weather-induced, hydrodynamic variability. *J. Mar. Syst.* 54, 139–155. doi: 10.1016/j.jmarsys.2004.07.009
- Nogueira, E., Ibáñez, F., and Figueiras, F. G. (2000). Effect of meteorological and hydrographic disturbances on the microplankton community structure in the Ría de Vigo (NW Spain). *Mar. Ecol. Prog. Ser.* 203, 23–45. doi: 10.3354/meps203023
- Nogueira, E., Pérez, F., and F. Ríos, A. (1997). Seasonal patterns and long-term trends in an estuarine upwelling ecosystem (Ría de Vigo, NW Spain). *Estuar. Coast. Shelf Sci.* 44, 285–300.
- Oakey, N. S. (1982). Determination of the rate of dissipation of turbulent energy from simultaneous temperature and velocity shear microstructure measurements. *J. Phys. Oceanogr.* 12, 256–271. doi: 10.1175/1520-0485(1982)012<0256:DOTROD>2.0.CO;2
- Obata, A., Ishizaka, J., and Endoh, M. (1996). Global verification of critical depth theory for phytoplankton bloom with climatological *in situ* temperature and satellite ocean color data. *J. Geophys. Res.* C 101, 20657–20667.
- Osborn, T. R. (1980). Estimates of the local rate of vertical diffusion from dissipation measurements. *J. Phys. Oceanogr.* 10, 83–89. doi: 10.1175/1520-0485(1980)010<0083:EOTLRO>2.0.CO;2
- Patti, B., Guisande, C., Vergara, A., Riveiro, I., Maneiro, I., Barreiro, A., et al. (2008). Factors responsible for the differences in satellite-based chlorophyll a concentration between the major global upwelling areas. *Estuar. Coast. Shelf Sci.* 76, 775–786. doi: 10.1016/j.ecss.2007.08.005
- Pitcher, G., Figueiras, F., Hickey, B., and Moita, M. (2010). The physical oceanography of upwelling systems and the development of harmful algal blooms. *Prog. Oceanogr.* 85, 5–32. doi: 10.1016/j.pocean.2010.02.002
- Prandke, H., Holtsch, K., and Stips, A. (2000). *MITEC Technology Development: The Microstructure/Turbulence Measuring System MSS*. ISPRA: Space Applications Institute.
- Prandke, H., and Stips, A. (1998). Test measurements with an operational microstructure-turbulence profiler: detection limit of dissipation rates. *Aquat. Sci.* 60, 191–209. doi: 10.1007/s000270050036
- Rosón, G., Cabanas, J. M., and Pérez, F. F. (2008). “Hidrografía y dinámica de la Ría de Vigo: un sistema de afloramiento,” in *La Ría de Vigo: Una Aproximación Integral al Ecosistema Marino de la Ría de Vigo*, eds A. González-Garcés, F. Vilas, and X. A. Álvarez-Salgado (Vigo: Instituto de estudios vigüeses), 111–152.
- Ross, O. N., and Sharples, J. (2004). Recipe for 1-d lagrangian particle tracking models in space-varying diffusivity. *Limnol. Oceanogr.* 2, 289–302. doi: 10.4319/lo.2004.2.289
- Rossi, V., López, C., Hernández-García, E., Sudre, J., Garçon, V., and Morel, Y. (2009). Surface mixing and biological activity in the four eastern boundary upwelling systems. *Nonlin. Process. Geophys.* 16, 557–568. doi: 10.5194/npg-16-557-2009
- Semina, H. J. (1960). The influence OP vertical circulation on the phytoplankton in the Bering Sea. *Int. Rev. Gesam. Hydrobiol. Hydrogr.* 45, 1–10. doi: 10.1002/iroh.19600450102
- Sharples, J., Moore, C. M., Hickman, A. E., Holligan, P. M., Tweddle, J. F., Palmer, M. R., et al. (2009). Internal tidal mixing as a control on continental margin ecosystems. *Geophys. Res. Lett.* 36, 1–5. doi: 10.1029/2009GL040683
- Sharples, J., Tweddle, J. F., Mattias Green, J. A., Palmer, M. R., Kim, Y.-N., Hickman, A. E., et al. (2007). Spring-neap modulation of internal tide mixing and vertical nitrate fluxes at a shelf edge in summer. *Limnol. Oceanogr.* 52, 1735–1747. doi: 10.4319/lo.2007.52.5.1735
- Siegel, D. A., Doney, S. C., and Yoder, J. A. (2002). The North Atlantic spring phytoplankton bloom and Sverdrup's critical depth hypothesis. *Science* 296, 730–733. doi: 10.1126/science.1069174
- Smyth, W. D. (2020). Marginal instability and the efficiency of ocean mixing. *J. Phys. Oceanogr.* 50, 2141–2150. doi: 10.1175/JPO-D-20-0083.1

- Sverdrup, H. U. (1953). On conditions for the vernal blooming of phytoplankton. *ICES J. Mar. Sci.* 18, 287–295. doi: 10.1093/icesjms/18.3.287
- Taylor, G. I. (1935). Statistical theory of turbulence. *Proc. R. Soc. Lond. Ser. A Math. Phys. Sci.* 151, 421–444. doi: 10.1098/rspa.1935.0159
- Taylor, J. R., and Ferrari, R. (2011). Shutdown of turbulent convection as a new criterion for the onset of spring phytoplankton blooms. *Limnol. Oceanogr.* 56, 2293–2307. doi: 10.4319/lo.2011.56.6.2293
- Teixeira, I., and Figueiras, F. (2009). Feeding behaviour and non-linear responses in dilution experiments in a coastal upwelling system. *Aquat. Microb. Ecol.* 55, 53–63. doi: 10.3354/ame01281
- Thakur, R., Shroyer, E. L., Govindarajan, R., Farrar, J. T., Weller, R. A., and Moum, J. N. (2019). Seasonality and buoyancy suppression of turbulence in the Bay of Bengal. *Geophys. Res. Lett.* 46, 4346–4355. doi: 10.1029/2018GL081577
- Torrence, C., and Compo, G. P. (1998). A practical guide to wavelet analysis. *Bull. Am. Meteorol. Soc.* 79, 61–78. doi: 10.1175/1520-0477(1998)079<0061:APGTWA>2.0.CO;2
- Torrence, C., and Webster, P. J. (1999). *Interdecadal Changes in the ENSO-Monsoon System*. American Meteorological Society.
- Townsend, D. W., Keller, M. D., Sieracki, M. E., and Ackleson, S. G. (1992). Spring phytoplankton blooms in the absence of vertical water column stratification. *Nature* 360, 59–62. doi: 10.1038/360059a0
- Vallina, S. M., and Simó, R. (2007). Strong relationship between DMS and the solar radiation dose over the global surface ocean. *Science* 315, 506–508. doi: 10.1126/science.1133680
- Villamaña, M., Maraño, E., Cermeño, P., Estrada, M., Fernández-Castro, B., Figueiras, F. G., et al. (2019). The role of mixing in controlling resource availability and phytoplankton community composition. *Prog. Oceanogr.* 178:102181. doi: 10.1016/j.pocean.2019.102181
- Villamaña, M., Mouriño-Carballido, B., Maraño, E., Cermeño, P., Chouciño, P., da Silva, J. C. B., et al. (2017). Role of internal waves on mixing, nutrient supply and phytoplankton community structure during spring and neap tides in the upwelling ecosystem of Ria de Vigo (NW Iberian Peninsula). *Limnol. Oceanogr.* 62, 1014–1030. doi: 10.1002/lno.10482
- Warner, S. J., Becherer, J., Pujana, K., Shroyer, E. L., Ravichandran, M., Thangaprakash, V., et al. (2016). Monsoon mixing cycles in the Bay of Bengal: a year-long subsurface mixing record. *Oceanography* 29, 158–169. doi: 10.5670/oceanog.2016.48
- Whalen, C. B., Talley, L. D., and MacKinnon, J. A. (2012). Spatial and temporal variability of global ocean mixing inferred from Argo profiles. *Geophys. Res. Lett.* 39, 1–6. doi: 10.1029/2012GL053196
- Wihsgott, J. U., Sharples, J., Hopkins, J. E., Woodward, E. M. S., Hull, T., Greenwood, N., et al. (2019). Observations of vertical mixing in autumn and its effect on the autumn phytoplankton bloom. *Prog. Oceanogr.* 177:102059. doi: 10.1016/j.pocean.2019.01.001

**Conflict of Interest:** The authors declare that the research was conducted in the absence of any commercial or financial relationships that could be construed as a potential conflict of interest.

**Publisher's Note:** All claims expressed in this article are solely those of the authors and do not necessarily represent those of their affiliated organizations, or those of the publisher, the editors and the reviewers. Any product that may be evaluated in this article, or claim that may be made by its manufacturer, is not guaranteed or endorsed by the publisher.

Copyright © 2021 Comesaña, Fernández-Castro, Chouciño, Fernández, Fuentes-Lema, Gilcoto, Pérez-Lorenzo and Mouriño-Carballido. This is an open-access article distributed under the terms of the Creative Commons Attribution License (CC BY). The use, distribution or reproduction in other forums is permitted, provided the original author(s) and the copyright owner(s) are credited and that the original publication in this journal is cited, in accordance with accepted academic practice. No use, distribution or reproduction is permitted which does not comply with these terms.